University of Alberta

Ultrafast, Third-order Nonlinear Optical Properties of As_2Se_3 Chalcogenide Glass

By

Andrzej Tomalik ©

A thesis submitted to the Faculty of Graduate Studies and Research
in partial fulfillment of the requirements for the degree of Master of Science

Department of Electrical and Computer Engineering

Edmonton, Alberta
Fall 2006

Library and Archives Canada

Published Heritage Branch

395 Wellington Street
Ottawa ON K1A 0N4
Canada

Bibliothèque et Archives Canada

Direction du Patrimoine de l'édition

395, rue Wellington
Ottawa ON K1A 0N4
Canada

Your file Votre référence
ISBN: 978-0-494-22388-8
Our file Notre référence
ISBN: 978-0-494-22388-8

NOTICE:
The author has granted a non-exclusive license allowing Library and Archives Canada to reproduce, publish, archive, preserve, conserve, communicate to the public by telecommunication or on the Internet, loan, distribute and sell theses worldwide, for commercial or non-commercial purposes, in microform, paper, electronic and/or any other formats.

The author retains copyright ownership and moral rights in this thesis. Neither the thesis nor substantial extracts from it may be printed or otherwise reproduced without the author's permission.

AVIS:
L'auteur a accordé une licence non exclusive permettant à la Bibliothèque et Archives Canada de reproduire, publier, archiver, sauvegarder, conserver, transmettre au public par télécommunication ou par l'Internet, prêter, distribuer et vendre des thèses partout dans le monde, à des fins commerciales ou autres, sur support microforme, papier, électronique et/ou autres formats.

L'auteur conserve la propriété du droit d'auteur et des droits moraux qui protège cette thèse. Ni la thèse ni des extraits substantiels de celle-ci ne doivent être imprimés ou autrement reproduits sans son autorisation.

In compliance with the Canadian Privacy Act some supporting forms may have been removed from this thesis.

While these forms may be included in the document page count, their removal does not represent any loss of content from the thesis.

Conformément à la loi canadienne sur la protection de la vie privée, quelques formulaires secondaires ont été enlevés de cette thèse.

Bien que ces formulaires aient inclus dans la pagination, il n'y aura aucun contenu manquant.

Canada

ABSTRACT

Chalcogenide glasses exhibit an ultrafast nonlinear optical (NLO) response making them excellent candidates for photonic switching devices at communication wavelengths around 1550nm.. While the nonlinear Kerr coefficient of As_2Se_3 has been studied by several groups, few studies have probed the temporal dynamics of the 3rd order nonlinear response in chalcogenide glasses. For ultrafast time-resolved measurements of Kerr dynamics in chalcogenide glass films, we have developed a wavelength-tunable, time-resolved, differential optical Kerr effect (DOKE) detection system. We have studied the NLO response of As_2Se_3 films deposited on BK-7 glass substrate by thermal evaporation. We observed a large Kerr response in films as thin as 4.5μm. The obtained Kerr coefficient for As_2Se_3, at $\lambda = 1425nm$, was $n_2 = 6.7\times10^{-18} m^2/W$, and a two-photon absorption coefficient $\beta = 0.14\times10^{-11} m/W$. The Kerr response follows the autocorrelation of the pulse and there was no evidence of a slow component in the decay.

ACKNOWLEDGEMENT

I would first like to thank my supervisors, Dr Ray DeCorby and Dr. Frank Hegmann. I thank Dr. DeCorby for quickly realizing my interests and finding me a research project that has kept me enthusiastic and motivated throughout. I particularly thank you, Ray, for being able to stay current with my progress, despite having a full schedule, thus giving me the necessary push to a successful completion. I thank Dr. Hegmann for providing me with the means for completing my project - his lab. Thank you, Frank, for keeping interest in my project from start to finish, and your willingness to always provide valuable feedback.

A very special thanks goes to Aaron Slepkov who, despite having his own work, always stuck by my side providing a helping hand, his expertise and, most importantly, his friendship, which will not be forgotten. Thank you, Aaron, for all your enthusiasm which I found to be quite contagious. Many thanks also goes to David Cooke who has volunteered hours of his time and his patience of steel to getting the lab equipment working. Thank you, David, for saving me countless hours of frustration.

Last, but definitely not least, I thank Tom Clement and Prabhat Dwivedi for preparing the glass samples, as well as the rest of my committee members, Dr. Rik Tykwinski, Dr. Vien Van, and Dr. John Salomon.

Generous funding was provided by TRLabs and CIPI.

TABLE OF CONTENTS

CHAPTER 1 *Introduction* **1**

Brief History of Nonlinear Optics and the Optical Kerr Effect **2**
All-Optical Switching Based on the Kerr Effect **4**
Kerr Effect Devices Based on Chalcogenide Glass **5**
Techniques for Measuring the Optical Kerr Effect **7**
Z-Scan **10**
Spectrally Resolved Two-Beam Coupling **13**
Degenerate Four-Wave Mixing **15**
Optical Homodyne Detection **18**
Optical Heterodyne Detection (OHD) **20**
Differential Optical Kerr Effect (DOKE) Detection Technique **21**
Thesis Goals and objectives **24**

CHAPTER 2 *Theory* **26**

Third-Order Susceptibility, $\chi^{(3)}$ **27**
Physical Contributions to Third-Order Nonlinearities **32**
Resonant versus Non-Resonant Nonlinearity **34**
Third-Order Nonlinearities in Chalcogenide Glasses **36**
Modeling the Kerr Coefficient in As_2Se_3 **38**

CHAPTER 3 *Differential Optical Kerr Gate Setup* **45**

Overview of the DOKE System **46**
DOKE Formulations **50**
DOKE Detection System **52**
Photodetectors **52**
Power Supply **57**
Photodetector Characterization and Calibration **59**
Temporal Alignment of the Pump and Probe Beams **67**

CHAPTER 4 *Setup Characterization and Results* **69**

Beam Diagnostics **70**
Spatial Beam Profile **70**
Beam Autocorrelation **73**
Kerr Gate Characterization **75**
DOKE Polarization Conditions **77**
Measurements on Carbon Di-sulfide (CS_2) **78**
Measurements on Fused Silica (SiO_2) **80**
Measurement Details **82**
Measurements on As_2Se_3 Films **84**
Sample Preparation **84**
Time-Resolved Scans **85**

CHAPTER 5 *Conclusions and Future Work* **92**

REFERENCES **96**

APPENDIX A *Derivation of DOKE Equations* **103**

APPENDIX B *Nonlinear Phaseshift Calculation* **108**

APPENDIX C *Calculations with Reference Sample* **110**

APPENDIX D *Sample Results and Calculations* **112**

LIST OF TABLES

TABLE 2.1 Linear and nonlinear index variation with composition variation in the As-S-Se glass system as reported by J. M. Harbold et al. [54]. **43**

TABLE 2.2 Reported results for As_2Se_3 glass. **44**

TABLE 4.1 DOKE experimental results. **90**

TABLE 4.2 Reported Kerr and two photon absorption coefficients for the As_2Se_3 in the 1400-1600nm wavelength range. **91**

TABLE A.1 Matrix representation of various optical elements used in the DOKE setup. **103**

TABLE D.1 Sample results recorded for consecutive Kerr scans of fused silica, thin film sample and film substrate. **113**

LIST OF FIGURES

FIGURE 1.1. All-optical switching with a) directional coupler, b) Mach-Zender interferometer, and c) microring resonator. **7**

FIGURE 1.2. Figure of merit as a function of the nonlinear transmission for phase shifts $\phi = \pi/2, \pi$ and 2π. To get more light through the device, a higher figure of merit is required to achieve the needed nonlinear phase shift [22]. **9**

FIGURE 1.3. Self - focusing effect. Weaker intensity induces minimal self-focusing (a). As the intensity increases, the self-focusing effect becomes larger (b). **11**

FIGURE 1.4. Z-scan experimental setup where power meter reading is recorded as a function of sample position z. **11**

FIGURE 1.5. Spectrally-resolved two beam coupling. **14**

FIGURE 1.6. Four photon interaction in four-wave mixing. **15**

FIGURE 1.7. Two-beam coupling. Interference of two waves in a medium creates a grating pattern. **16**

FIGURE 1.8. Degenerate four-wave mixing in a nonlinear medium. Pump beam 2, counter propagating to pump beam 1, is Bragg reflected along the probe beam creating its conjugate wave. **17**

FIGURE 1.9. Degenerate four-wave mixing experimental setup [25]. **17**

FIGURE 1.10. Homodyne detection experimental setup. **19**

FIGURE 1.11. Heterodyne detection experimental setup. **21**

FIGURE 1.12. DOKE detection experimental setup. **22**

FIGURE 1.13. The curve represents the light transmitted through the polarizer-analyzer pair, at an angle from the fully crossed condition. The detection ranges for Homodyne, OHD and DOKE techniques are comparatively shown along the curve. **24**

FIGURE 2.1. Nuclear response function of the 20% Nb_2O_5-80% TeO_2 glass sample ob-

tained using a time-resolved heterodyne optical Kerr effect technique [39]. **33**

FIGURE 2.2. Frequency of operation maximizing the Kerr nonlinearity, relative to the material bandgap. The linear and nonlinear absorption is minimized by operating between the half-gap and the third-gap. **36**

FIGURE 2.3. Theoretical prediction of spectral dependence of n_2 in As_2Se_3 glass. The upper two curves are based on the Sheik-Bahae (S-B) model (eqns. 2.21 and 2.22), and the lower two curves are based on the single oscillator (S.O.) model (eqns. 2.20 and 2.23) [61]. **41**

FIGURE 3.1. Schematic diagram of the differential optical Kerr effect (DOKE) experimental setup **46**

FIGURE 3.2. Schematic diagram of the beam attenuator. Unwanted leakage of the original polarization passes through the polarizer thus degrades our signal (a). This leakage signal is blocked by crossing the polarizer with the original polarization (b). Rotating the half-wave plate between θ=0° and θ=45° gives us the full range of intensity control. **48**

FIGURE 3.3. Photodetector circuit schematic utilizing a low noise transimpedance amplifier in a photoconductive mode. **53**

FIGURE 3.4. Schematic diagram of (a) summing amplifier and (b) difference amplifier. **55**

FIGURE 3.5. Circuit diagram of the differential detection system employing two transimpedance amplifiers (one for each signal A and B), and unity gain summing and difference amplifiers. **57**

FIGURE 3.6. Diagram of the power supply for the detection circuit. **58**

FIGURE 3.7. Plot of the photodetector response to varying laser intensity. We plotted the response of photodetector "A" vs. "B", "A" vs. "Ref" and "B" vs. "Ref" to verify linear response. Each plot is fitted to a line. **60**

FIGURE 3.8. Plot of the photodetector response to varying laser intensity. Plotted is the response of photodetector "A" and "B" vs. a Newport power meter. To demonstrate linear response, each plot is again fitted to a line. **61**

FIGURE 3.9. Differential photodetector. Plot of signals "A-B" vs. "A"-"B" **63**

FIGURE 3.10. Relation between the pump and the probe signal references. **64**

FIGURE 3.11. OPA laser intensity fluctuates by as much as 20% in this case. Much of this noise can be eliminated with the use of a reference detector. **66**

FIGURE 3.12. Visible spot pattern through β-BBO crystal at zero pump-probe time delay. When the pulses are not aligned in time, only the two outer spots are present. **68**

FIGURE 4.1. Spatial profile of (a) the pump and (b) the probe beams. The pump beam is circular with a spot size of about 590μm. The probe beam is elongated in one direction with ω_1 = 320μm and ω_2 = 204μm. **71**

FIGURE 4.2. Kerr signal showing the autocorrelation of the pulse observed in a sample of fused silica. The pulse duration is 125fs at FWHM. **74**

FIGURE 4.3. DOKE signal versus pump intensity. The test was performed using a sample of (a) fused silica and (b) carbon disulfide (CS_2) solution. **75**

FIGURE 4.4. DOKE signal for a sample of CS_2 obtained at the four different pump beam polarization conditions at λ=1390nm. **77**

FIGURE 4.5. Time-resolved Kerr scan of CS_2 at λ=1390nm, showing a double-peak and an exponential decay response indicating electronic and molecular orientational contributions to the Kerr signal. Inset trace is a log plot of the result showing the relaxation time, t =1.59 ps, in the decay tail. **79**

FIGURE 4.6. Time-resolved Kerr scan of SiO_2 at λ=1425nm. From the symmetric Gaussian shape, which represents the autocorrelation of the laser pulse, it is evident that the Kerr response is purely electronic. **80**

FIGURE 4.7. Transmission spectrum of As_2Se_3[73] **85**

FIGURE 4.8. DOKE Kerr scan of As_2Se_3, 4.5μm thick (top) and 16μm thick (bottom) films deposited on BK-7 glass, at a wavelength λ=1425nm. DOKE scan of the corresponding BK-7 substrate alone is included in the inset. **87**

FIGURE 4.9. DOKE nonlinear absorption scan (pump polarization θ=0°) of the 16μm, As_2Se_3 film deposited on BK-7 glass, at a wavelength λ=1425nm. The fused silica zero reference scan is included in the inset. **89**

LIST OF ABBREVIATIONS

NLO	Nonlinear optics/optical
FOM	Figure of merit
DOKE	Differential optical Kerr effect
OPA	Optical parametric amplifier
MASER	Microwave amplification by stimulated emission radiation
IR	Infra-red
NOLM	Nonlinear optical loop mirror
TPA	Two-photon absorption
SRTBC	Spectrally resolved two-beam coupling
DFWM	Degenerate four wave mixing
OHD	Optical heterodyne detection
S.O.	Single oscillator
S-B	Sheik-Bahae model
BBAR	Broadband anti-reflection coating
PC	Personal computer
FWHM	Full-width-half-maximum
SPM	Self-phase modulation

CHAPTER 1

Introduction

In 1818 Fresnel wrote a letter to the French Academy of Sciences in which he noted that the proportionality between the vibration of light and the subsequent vibration of matter was only true because no high intensities were available [1]. It was not until the invention of the laser in 1960's that Fresnel's assertion could be verified. With lasers providing intensities much higher then previously possible, many experiments that followed led to the observations of interphoton interactions in optical media, and made it clear that optical media exhibit nonlinear behavior and light can be used to control light [2]. The field of nonlinear optics comprises many fascinating phenomena and has revolutionized many areas of research. The optical Kerr effect is one such nonlinear property that is common to all materials. The large optical Kerr effect of certain optical materials is of interest

within photonic telecommunications as a mechanism for achieving all-optical switching [2].

1.1 Brief History of Nonlinear Optics and the Optical Kerr Effect

The beginnings of the laser date back to 1954 when Charles H. Townes, James P. Gordon and Herbert J. Zeiger built the first MASER (Microwave Amplification by Stimulated Emission Radiation) at Columbia University. The MASER used ammonia (NH_3) as an active gain medium to produce coherent microwave radiation [3]. Two years later, Nicolaas Bloembergen's work in electron spin resonance led to his invention of the three-level solid-state maser [4]. Bloembergen's work provided the fundamentals for the subsequent developments in laser technology, which rely most heavily on the three-level pumping system. In 1958, Arthur L. Schawlow and Charles H. Townes published a paper entitled "Infrared and Optical Masers" [3], in which they proposed to extend the principles of masers into the visible region of the spectrum. While theoretical physicists wrote papers and debated the merits of different materials and approaches for a laser, Maiman set out to build one [5]. In 1960, using the three-level principle worked out by Bloembergen, Theodore Maiman constructed the first operational laser on the 16th of May 1960, at the Hughes Research Laboratory in California. Maiman observed a monochromatic beam of radiation by shining a high power flash lamp on a synthetic ruby rod with silver-coated surfaces [6][7]. Since Maiman used a pulsed light source to excite the ruby, his laser produced only short flashes of light rather than a continuous wave. It also produced larger than anticipated power since substantial energy was released during a short time. Not too

long after this, a technique known as "Q switching" was introduced at the Hughes Laboratory [6], further shortening the pulse and increasing peak powers above the mega-watt level. The availability of pulsed, high intensity laser light shortly thereafter led to the discovery of second-harmonic generation by Franken *et al.* in 1961 [8]. This was the beginning of the modern area of research in the field of nonlinear optics. The field of nonlinear optics also has roots in research in electro-optics which dates back to mid 1800s and John Kerr's work concerning the effect of electric and magnetic fields on light [8][9][10].

John Kerr was a Scottish physicist who first began work in the field of electro-optics. Born in Ardrossan, Ayrshire, John Kerr received a Master of Arts in Physical Science with highest distinction from the Glasgow University. Kerr was also interested in religion and took a theology degree before becoming an ordained minister of the Free Church of Scotland. Instead of practicing as a minister, however, he accepted a position as a lecturer in physical science and mathematics with the Glasgow Free Church Teacher Training College, where he continued teaching for over 40 years. He retained his interest in science and set up a small laboratory where he pursued his research interests [9]. He performed experiments of great precision to measure very small effects, and it was in his laboratory that he discovered an electro-optic effect later known as the Kerr effect. Utilizing a simple slab of glass, an induction coil with two metal probes, and a polarizer and an analyzer in crossed orientation, Kerr observed that the light passing through is doubly refracted when an electric field is applied to the optical medium. In other words, Kerr observed that a strong electric field causes the structure of the glass to alter causing a difference in refractive index for light polarized in the plane of the field and light polarized normal to it. This effect is known as birefringence. He designed what was to become known as the Kerr cell

and, using it, he found that the induced birefringence is directly proportional to the square of the applied electric field [8][9][10]. The Kerr cell was subsequently exploited in applications such as high-speed photography, with shutter speeds as fast as 100ns. In 1928 Karolus and Mittelstaedt used a Kerr cell to modulate a beam of light in order to measure its speed [10]. The Kerr cell provided modulation frequencies of approximately10MHz, greatly improving the precision of the experiment compared to earlier attempted mechanical means of modulation which were limited to modulation frequencies of around 10kHz [10].

The invention of the laser led to the discovery of a special case of the Kerr effect, where electric fields associated with high intensity light directly produce a change in the optical properties of a medium. Because of its similarity to the electro-optic Kerr effect, this effect became known as the optical Kerr effect [2]. Today, the Kerr effect is exploited by numerous researchers in areas such as generation of ultrashort laser pulses and very high speed switching in telecommunication devices [8].

1.2 All-Optical Switching Based on the Kerr Effect

Switching is an essential operation of communication networks and is also the basic operation in digital computers and signal processing systems. With current electronic technology approaching fundamental size and speed limits, scientists are looking into high-speed photonic switches for solutions to the ever-increasing demand for communication and processing bandwidth. The photonic technology, however, continues to experience technical difficulties and technological immaturity. The requirements for photonic switching

devices include low switching energies, high-speed response, low loss and compatibility with existing fiber technology [11]. Meeting these requirements is not a simple task and one of the most promising approaches relies on employing an optical nonlinearity such as the Kerr effect. Fiber devices employing the Kerr effect have the potential of reaching transmission rates in the range of Tbits/s [12]. However, the weak nonlinearity of oxide optical fibers limits the practical implementation of all-optical switching devices mainly because of long interaction length and high switching powers required. Considerable effort has been devoted to the design and characterization of materials and devices that would yield low switching energies along with high-speed response. Many materials, including organic materials [13], semiconductors [1], and glasses [14] were explored as candidates for all optical switching (AOS).

1.3 Kerr Effect Devices Based on Chalcogenide Glass

Much effort has been devoted to the study of glasses containing chalcogens (Sulfur (S), Selenium (Se), Tellurium (Te)), which are among the most nonlinear glasses known [11]. They are highly transparent in the near infra-red (IR) region, they demonstrate ultra fast response times well below 1ps, and are easier to fabricate as waveguide structures than single-crystal semiconductors. The optical properties of chalcogenide glasses, such as the effective bandgap and linear refractive index, can be carefully engineered [11] in an effort to maximize the Kerr nonlinearity and to give the optimal performance at the communication wavelengths around 1550nm [11][15]. Large Kerr nonlinearity in chalcogenide materials is being exploited for all-optical signal processing in high-speed optical communication

systems, allowing the creation of all-optical switches, supercontinuum generators, and all-optical regenerators [16][17]. Such devices have the key advantage that bandwidth is limited only by the intrisnic material nonlinear response, and can greatly exceed the fundamental limits (about 40Gb/s) of electronic processing speeds. The low optical nonlinearity of silica glass means that a significant nonlinear response at low laser pulse power can be achieved only after propagation through hundreds of meters of silica fiber. However, for practical applications much more compact, chip-scale integrated devices are desirable. Principles of ultrafast nonlinear switching and basic logic operations have been demonstrated with numerous photonic devices that employ chalcogenide glass as the nonlinear medium. Such photonic devices include Mach-Zender interferometers [18], directional couplers [12], micro-ring resonators [19], nonlinear optical loop mirrors (NOLMs) [20], and photonic bandgap structures [21]. The small waveguide cross-sectional dimensions of chalcogenide-based waveguides helps to keep a high power density within the nonlinear interaction length, thus keeping the average switching powers relatively low.

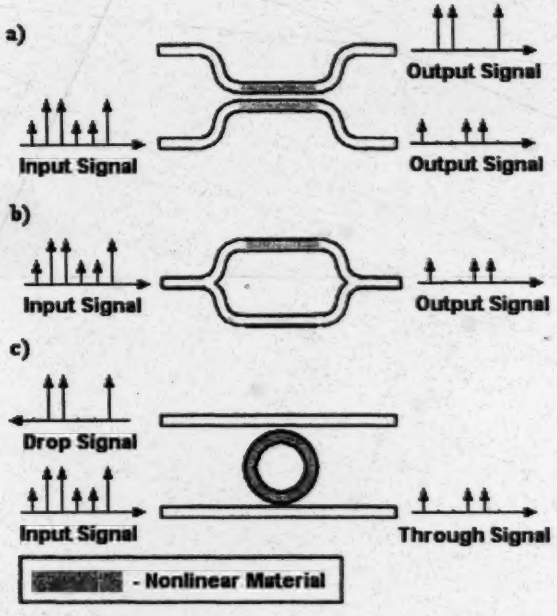

FIGURE 1.1. All-optical switching with a) directional coupler, b) Mach-Zender interferometer, and c) microring resonator.

Before we can design an effective all-optical switch, however, a better understanding of the Kerr effect dynamics in chalcogenide glasses is required.

1.4 Techniques for Measuring the Optical Kerr Effect

The Kerr effect is a third-order optical nonlinearity that corresponds to an intensity-dependent refractive index change. The variation of the refractive index of a medium is proportional to the local optical intensity as given by Equation 1.1,

$$n(I) = n_o + n_2 I, \qquad \text{(Eq. 1.1)}$$

where n_o is the linear index of refraction, I is the incident light intensity in (W/m^2) and n_2 is the nonlinear index of refraction in (m^2/W). The nonlinear index of refraction is referred to as the Kerr coefficient . This intensity dependent modulation of the refractive index is the basic operating principle in most all-optical switching devices.

Always accompanying the intensity-dependent change of refractive index is an intensity dependent absorption, $\alpha(I)$, given by

$$\alpha(I) = \alpha_o + \beta I, \qquad \text{(Eq. 1.2)}$$

where α_o is the linear absorption in (m^{-1}) and β is the nonlinear, two-photon absorption (TPA) coefficient in (m/W).

For a Kerr medium to be useful for optical signal processing devices, it must satisfy a number of conditions. In order to keep switching energies at feasible levels, the material must possess a strong Kerr nonlinearity. This implies that we would like the nonlinear coefficient (n_2) to be as large as possible. At the same time, the excitation time of the nonlinear effect must be shorter then the pulse width and the sum of excitation and relaxation times must be shorter than the pulse spacing. This will ultimately determine the maximum switching speeds. The effect of linear and nonlinear absorption must be weak at the wavelength of interest. This means that we require a highly transparent medium with nonlinear absorption coefficient, β, as small as possible in order to minimize signal attenuation. Considering the above arguments, a common figure of merit (FOM) is as follows [22]:

$$FOM = \frac{n_2}{\beta\lambda}, \qquad \text{(Eq. 1.3)}$$

where λ is the vacuum wavelength of light. The design of an efficient all-optical switch requires a material where the nonlinearity per unit nonlinear absorption, as embodied by the figure of merit in Equation 1.3, is large. Intuitively, we are trying to accumulate nonlinear phase shift while propagating in the waveguide, but at the same time are losing intensity to TPA making it more difficult to accumulate additional nonlinear phase. This means that to achieve some nonlinear phase, we have to trade-off the figure of merit to total intensity transmission as shown in Figure 1.2.

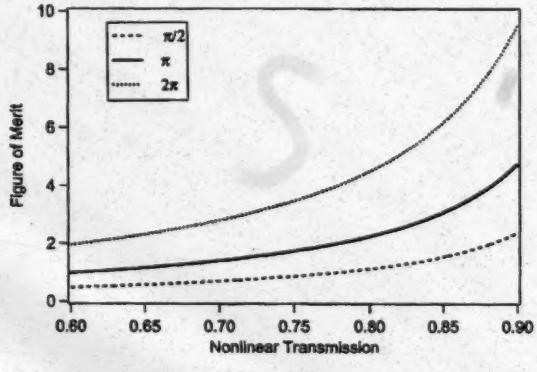

FIGURE 1.2. Figure of merit as a function of the nonlinear transmission for phase shifts $\phi = \pi/2$, π and 2π. To get more light through the device, a higher figure of merit is required to achieve the needed nonlinear phase shift [22].

Typically, an all-optical switching criteria requires a material to posses a figure of merit $FOM > 1$.

To study the Kerr effect dynamics in various optical media, a number of techniques have been developed over the years. Some of the more popular techniques include the z-scan [23], spectrally resolved two beam coupling (SRTBC) [24], degenerate four wave mixing (DFWM) [25], optical homodyne and heterodyne detection [26], and the differential optical Kerr effect detection (DOKE) [27] technique used in this work.

1.4.1 Z-Scan

Z-scan is a simple, single beam technique for measuring the sign and magnitude of the nonlinear refractive index (n_2) of optical materials. This technique takes advantage of the "self-focusing" and "self-defocusing" effects exhibited in nonlinear Kerr materials with a positive and negative n_2 coefficients (see Equation 1.1), respectively .

Consider a sample placed in the path of a focused laser beam. As the sample is moved towards the focus, the beam intensity inside the sample increases, leading to a self focusing effect in the sample. The intensity profile of an intense, Gaussian beam passing through a thin sheet of nonlinear, Kerr material, maps out a refractive index gradient in the transverse plane of the medium. For example, if the beam has highest intensity at the centre, the medium will exhibit maximum index change at that point. Consequently, a wave travelling though this graded-index medium exhibits a nonuniform phase shift causing wavefront curvature. The medium then acts as a lens with a power-dependent focal length [2]. This is demonstrated in Figure 1.3.

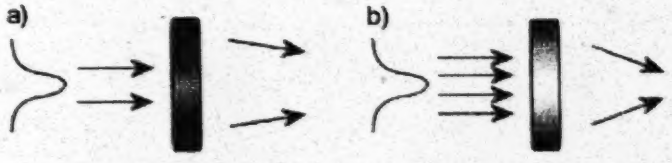

FIGURE 1.3. Self - focusing effect. Weaker intensity induces minimal self-focusing (a). As the intensity increases, the self-focusing effect becomes larger (b).

A typical, Z-scan experimental arrangement is shown in Figure 1.4. It uses a tightly focused Gaussian laser beam to measure the transmittance of a nonlinear material through a finite aperture in the far field as a function of the sample position (z) from the focal plane.

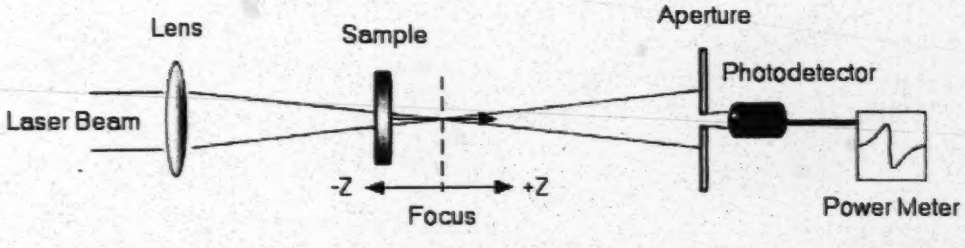

FIGURE 1.4. Z-scan experimental setup where power meter reading is recorded as a function of sample position z.

Starting the scan far from the focus (negative z) the beam intensity is relatively low and negligible beam focusing through the sample occurs. As the sample is brought closer to

the focus, the beam intensity increases leading to increasing self-focusing effect by the sample. A sample with positive n_2 will further focus the beam as it moves towards the focus, causing an increase in beam divergence at the aperture, hence a decrease in transmittance. Similarly, continuing a scan past the focus point (positive z), the same focusing will now tend to collimate the beam, causing beam narrowing at the aperture and an increase in transmittance. The opposite occurs for samples with negative n_2. Observing the prefocal and postfocal features of the scan immediately yields information about the sign of the nonlinearity. A prefocal transmittance minimum (valley) followed by a post focal maximum (peak) is the Z-scan signature of a positive n_2; the opposite is true for a negative n_2. The magnitude of n_2 is numerically obtained from the difference between the normalized peak (maximum) and valley (minimum) transmittances [28][29][30].

Removing the far-field aperture, thus collecting all the transmitted light, completely eliminates the above described effect, making the setup sensitive to nonlinear absorption. Now, scanning the sample through the focus in similar fashion yields a nonlinear absorption profile from which the two-photon absorption coefficient β may be calculated [28].

Z-scan is a simple technique, however, in comparison to other techniques, it suffers from poor sensitivity caused by unavoidable linear scatter from the sample as it traverses the beam focus [24]. Also, thermal effects pose a problem when a high repetition rate laser system is used with this technique. As the sample's temperature incrases, thermal nonlinearities arise from a change in the refractive index. Thermal nonlinearities are undesirable for applications of all-optical switching due to their long excitation and relaxation times. A laser with a very low repetition rate (~10 Hz) is required in this case in order to prevent

thermal effects from obscuring the results [31]. Alternately, a pump and probe Kerr detection technique offers insensitivity to slow reacting mechanisms such as thermal effects, as well as much improved Kerr detection sensitivity [24]. Also, for photonic applications, Kerr measurements of optical glasses should address not only the magnitudes of Kerr (n_2) and TPA (β) coefficients but also the Kerr temporal dynamics which can be obtained by time resolved Kerr scans as offered by techniques such as spectrally resolved two-beam coupling (SRTBC), degenerate four wave mixing (DFWM), optical homodyne and heterodyne, and differential optical Kerr effect (DOKE).

1.4.2 Spectrally Resolved Two-Beam Coupling

The SRTBC experiment is a standard pump and probe experiment and is illustrated in Figure 1.5. An intense, pump beam passes through the sample inducing a nonlinear index change according to Equation 1.1. By cross-phase modulation, this causes the weak probe beam passing through the sample to undergo a nonlinear phase shift. This nonlinear phase shift is sensed as a change in power at the output of a monochromator tuned to a fixed wavelength. Data is collected at the output of the monochromator as the delay between the pump and probe signals is varied in small increments as to record the material's response as a function of time [32].

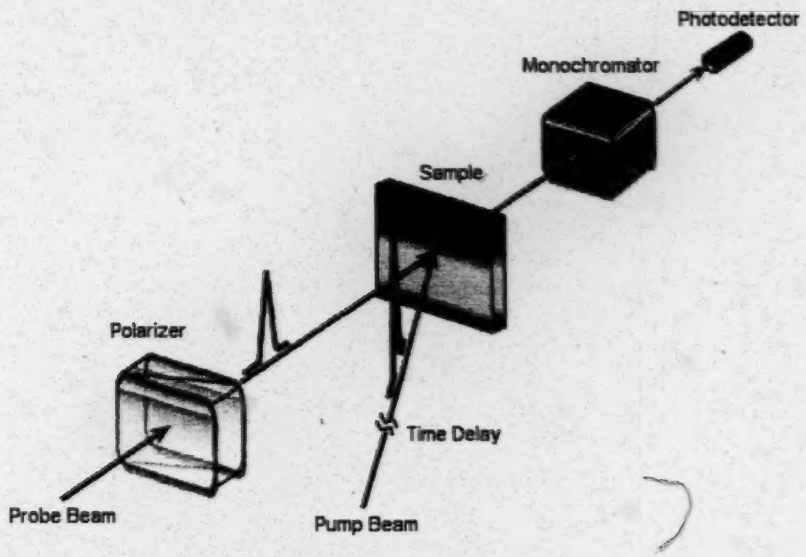

FIGURE 1.5. Spectrally-resolved two beam coupling.

For instantaneous response the nonlinear phase shift follows the temporal envelope of the pump pulse (pulse autocorrelation), whereas for a non-instantaneous response time the phase shift will be the convolution of the response function and the temporal envelope of the pump pulse. Hence, observation of the time-dependent nonlinear phase shift provides information about the material's Kerr dynamics [33]. By spectrally resolving the probe pulse, we can detect the transient signal at wavelengths where the fractional changes are the largest, thus maximizing the sensitivity. Measurements of n_2 will be most sensitive at monochromator wavelengths at the edges of the probe spectrum since the fractional spectral changes are the largest there [24].

The Kerr and two-photon absorption (TPA) coefficients may then be obtained by fitting the experimental results to a numerical solution for the nonlinear transmittance [24].

1.4.3 Degenerate Four-Wave Mixing

The four-wave mixing process may be interpreted as an interaction between four photons. A photon of frequency ω_1 combines with a photon of frequency ω_2 to produce a photon of frequency ω_3 and another of frequency ω_4 [2]. This is demonstrated in Figure 1.6.

$$\omega_1 + \omega_2 = \omega_3 + \omega_4 \qquad \text{(Eq. 1.4)}$$

$$k_1 + k_2 = k_3 + k_4 \qquad \text{(Eq. 1.5)}$$

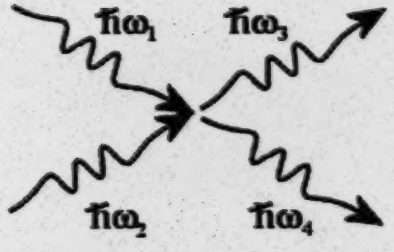

FIGURE 1.6. Four photon interaction in four-wave mixing.

A degenerate case of the process occurs when all four waves are of the same frequency.

$$\omega_1 = \omega_2 = \omega_3 = \omega_4 = \omega. \qquad \text{(Eq. 1.6)}$$

This process is then called degenerate four-wave mixing [2].

Let us consider a scenario of two beams of light (pump and probe) incident on a nonlinear material as shown on Figure 1.7. The interference of the two waves causes periodic intensity variations in the medium, which, in a Kerr medium, will form a refractive index grating [34].

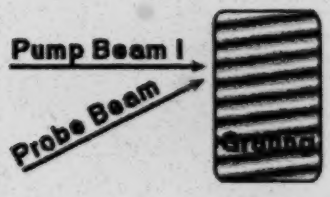

FIGURE 1.7. Two-beam coupling. Interference of two waves in a medium creates a grating pattern.

If we introduce another pump wave that is propagating in the opposite direction to the first pump wave ($k_1 = -k_3$), the wave will be Bragg diffracted by the intensity induced grating to create the conjugate wave; a wave that is reflected onto the probe wave ($k_2 = -k_4$) regardless of the angle of incidence of the probe wave, thus satisfying the phase matching condition in Equation 1.5 [2]. The four wave interaction in a medium is shown in Figure 1.8. Figure 1.9 illustrates a typical DFWM setup.

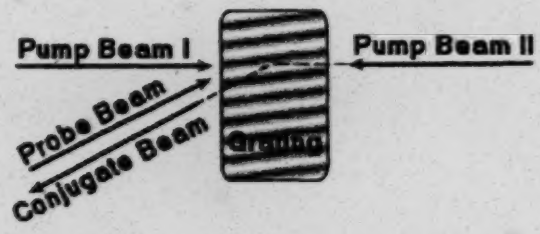

FIGURE 1.8. Degenerate four-wave mixing in a nonlinear medium. Pump beam 2, counter propagating to pump beam 1, is Bragg reflected along the probe beam creating its conjugate wave.

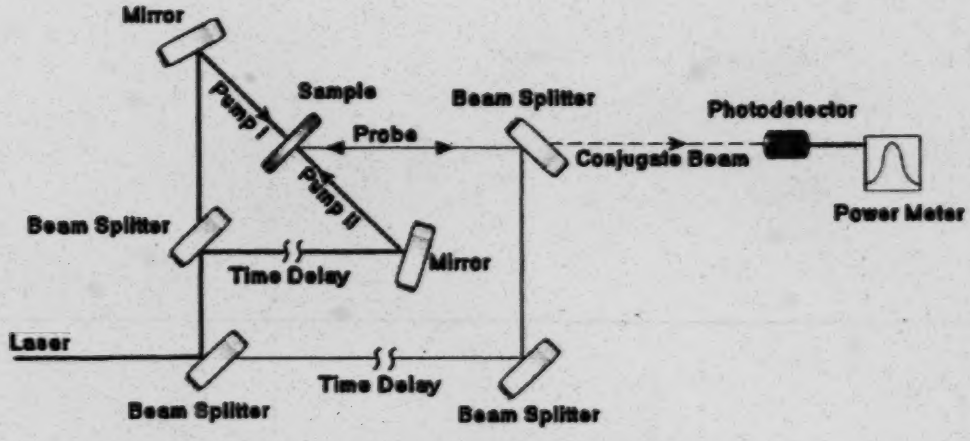

FIGURE 1.9. Degenerate four-wave mixing experimental setup [25].

The three beams, two counter-propagating pump beams (E_1 and E_2) and a probe beam (E_3), are incident on the sample as shown in Figure 1.8. The backward-directed, conjugate

wave (E_{out}) is sensed with a power meter or an oscilloscope. Its intensity is proportional to the nonlinear coefficient n_2, and the product of the field strengths of the three generating beams. Knowing the properties of the three beams, the value of the nonlinear coefficient n_2 may be extracted [25].

$$E_{out} \propto n_2 E_1 E_2 E_3 \qquad \text{(Eq. 1.7)}$$

The need for precise spatial and temporal alignment of all three beams makes this technique prone to alignment errors. In order to obtain absolute magnitude of the nonlinear coefficients, a material of known n_2 is usually required for reference with this technique [25]. The setup also introduces added complexity due to the need for three separate beams and two variable time delay lines for temporal alignment. In terms of data analysis, simple, analytic solutions for this setup are only possible when long probe delay times (comparable to or longer that the laser pulse length) are employed. When all the beams are incident simultaneously and coherently on a medium, a description in terms of multiple holograms is necessary for proper analysis. This leads to the coupled equation formalism and the temporal integrations involved in this case can only be performed numerically. In addition, since conjugate signal intensities can approach that of the pump, pump depletion effects may also have to be taken into account, complicating the calculations even further [35].

1.4.4 Optical Homodyne Detection

In a standard homodyne Kerr gate, a linearly polarized pump beam incident on a sample induces a change in refractive index along the axis of the polarization of the beam, making

the material birefringent ($\delta n = \delta n_{\parallel} - \delta n_{\perp}$). This dynamically induced birefringence can be sensed by a weak probe beam, polarized 45° to the pump beam. The change in refractive index manifests as a rotation of the polarization of the probe beam, which can be detected with the aid of a post-sample analyzer. Varying the time delay between the pump and the probe signal yields a time-resolved excitation profile [36][37][38]. The setup is demonstrated in Figure 1.10.

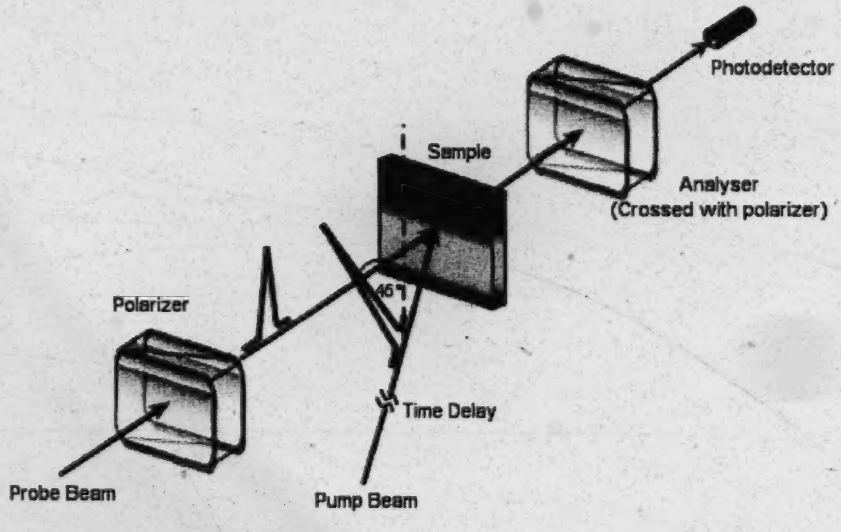

FIGURE 1.10. Homodyne detection experimental setup.

The downside to the detection based on fully crossed polarizers is that minimal light leakage or scatter transmitted to the photodetector through the analyser, greatly impairs the detection sensitivity. The detected signal is very small and may be of the order comparable to typical noise levels. Furthermore, the detected signal is proportional to the square of the

pump intensity, hence this technique is unable to separate the real and imaginary components of χ_3, namely the n_2 and β coefficients. In order to address this problem, an optical heterodyne detection technique is used by the majority of researchers [27][36][37][39].

1.4.5 Optical Heterodyne Detection (OHD)

This technique works on similar principles as the optical homodyne detection technique, with a small alteration introduced. In an attempt to improve the detection sensitivity of the homodyne technique, and separate the real and imaginary components of χ_3, the optical heterodyne detection system allows for a small amount of 90° out-of-phase light to be added to the probe signal. This is done by inserting a quarter-wave plate in the path of the probe, between the first polarizer and the sample, with its fast axis parallel to the transmission axis of the polarizer. Then, by slightly rotating the polarizer, a small amount of light perpendicularly polarized to the original probe, passes through to the sample. Now, since the polarizer and the analyzer are no longer fully crossed a small amount of light is detected even when no Kerr signal is present. This eliminates signal detection errors due to light leakage through fully crossed polarizers. The slightly uncrossed polarizers also allow this scheme to work in the regime where the detected signal is linear with pump intensity. This way, the heterodyne detection technique affords a larger dynamic range then the homodyne detection technique, and is able to isolate the real part of the nonlinear response directly from the Kerr signal [27][36][37][39].

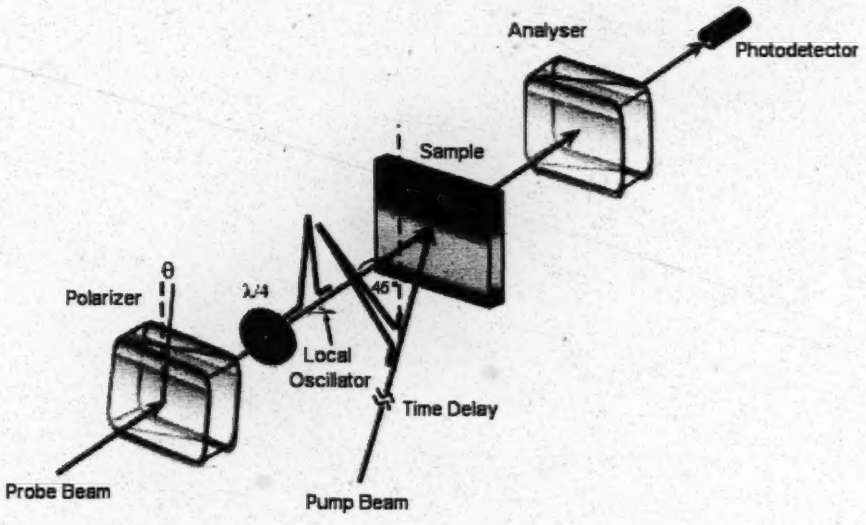

FIGURE 1.11. Heterodyne detection experimental setup.

1.4.6 Differential Optical Kerr Effect (DOKE) Detection Technique

The DOKE technique, much like the homodyne and heterodyne Kerr detection techniques, is a pump and probe technique. The major difference, however, is that it uses a circularly polarized probe beam and two (differential pair) photodetectors, "A" and "B". A quarter-wave plate after the first polarizer is placed such that the probe beam becomes circularly polarized. The post-sample analyzer then separates the orthogonal polarizations of the probe beam, and the transmitted and rejected beams are detected separately by the differential photodetectors.

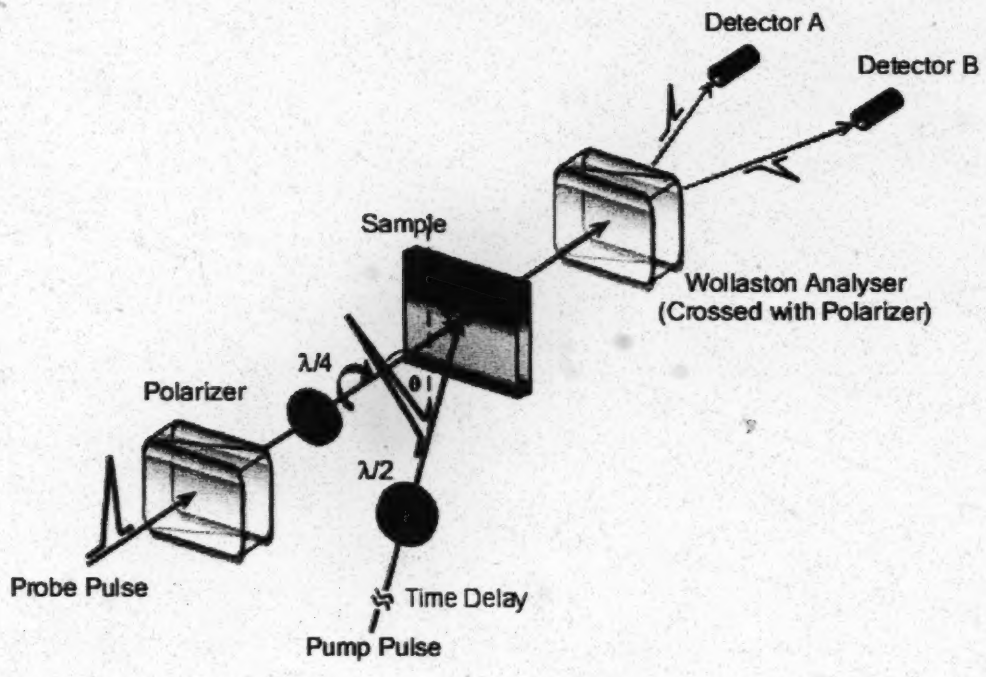

FIGURE 1.12. DOKE detection experimental setup.

The pump beam is polarized at 45° to the original (pre-quarter-wave plate) polarization of the probe beam. In the presence of a Kerr signal, with the pump beam chopped with a 50% duty cycle optical chopper, we detect an amplitude modulation of the probe beam with a modulation frequency corresponding to the chopper frequency. The detected "A-B" signal represents the magnitude of the Kerr signal. Controlling the time delay of the pump beam we are able to record a time resolved Kerr response with a resolution only limited by the

pulse width of the laser system. When the pump beam is polarized vertically (parallel to the pre-quarter-wave plate polarization of the probe), the detected signal provides information about the nonlinear (two-photon) absorption of the material. Thus, by alternating between the two pump polarization conditions, we are able to find both the Kerr (n_2) and TPA (β) coefficients. Working with a circularly polarized probe beam and differential photodetectors, the DOKE layout affords superior sensitivity, a larger linear dynamic range, as well as simplified analysis in comparison with most other Kerr gate schemes [27]. The detection range of the DOKE technique is qualitatively demonstrated in Figure 1.13, which shows a comparison to other Kerr gate schemes. The DOKE experimental setup is shown in Figure 1.12, and will be discussed in detail in Chapter 3.

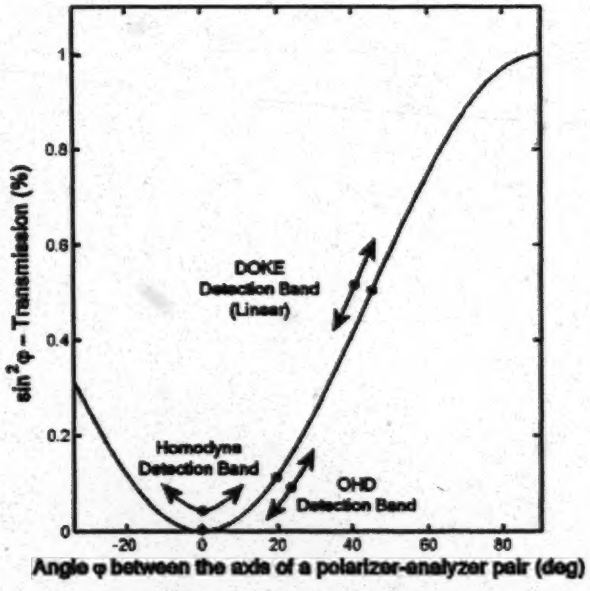

FIGURE 1.13. **The $\sin^2\varphi$ curve represents the light transmitted through the polarizer-analyzer pair, at an angle φ from the fully crossed condition. The detection ranges for Homodyne, OHD and DOKE techniques are comparatively shown along the curve.**

1.5 Thesis Goals and objectives

This work presents a study of third-order optical nonlinearities of thin film As_2Se_3 glass, where not only the magnitude but also the dynamics of the Kerr and two-photon absorption response are observed. For the study, a wavelength tunable DOKE detection setup was designed, built and tested. It is capable of examining the nonlinear Kerr coefficient n_2, two-photon absorption coefficient β, as well as temporal dynamics of the Kerr response in

thin film samples, in the 1250nm - 1600nm wavelength range. Following a theory section covering third-order optical nonlinearities, the details of the DOKE setup are given with the goal of presenting proof of proper system operation. This includes physical and mathematical descriptions of DOKE detection, hardware design considerations, and encountered problems. Finally, an experimental study of thin film As_2Se_3 glass samples is described.

CHAPTER 2

Theory

The linear properties of optical materials are relatively familiar; in the linear approximation, the refractive index is a fixed, intensity independent property of an optical medium. The refractive index arises from the perturbation of a polarization response in a medium in response to incident electromagnetic radiation. Consequently, the index of refraction modifies the phase velocity, the group velocity and the amplitude of the optical electromagnetic field within the medium. At optical frequencies, a major contribution to the dipole response of a medium is the oscillation of electron clouds around atomic nuclei. As long as the field driving the oscillation is small compared to the electric field that binds the electron cloud to he nucleus, the response is linear. If the incident electric field, on the

other hand, approaches that of the binding electric field, the oscillations become nonlinear. The nonlinear response χ^{NL} scales approximately as:

$$\chi^{NL} \sim \frac{E_{incident}}{E_{atomic}}. \qquad \text{(Eq. 2.1)}$$

For a hydrogen atom, for example, $E_{atomic} = 3\times10^{10}(V/m)$ [40]. Such high electric fields can be achieved at the focus of a laser beam, however, intensities of this magnitude will ionize the medium forming a plasma and damaging the material. A solution is to use the coherent property of laser light and much lower intensities. Each wavelength of propagation will generate a small nonlinear response which can add coherently over many wavelengths resulting in a large overall nonlinear response. The nonlinear response then scales as

$$\chi^{NL} \sim \frac{L}{\lambda}\frac{E_{peak}}{E_{atomic}}, \qquad \text{(Eq. 2.2)}$$

where L is the interaction length and λ is the wavelength of laser radiation. This type of nonlinear response can be utilized for nonlinear photonic applications [40].

2.1 Third-Order Susceptibility, $\chi^{(3)}$

At low electric fields a dielectric medium can be characterized by a linear relation between the polarization density, $\vec{P}$, and the electric field, $\vec{E}$, according to:

$$\vec{P} = \varepsilon_o \chi \vec{E}, \qquad \text{(Eq. 2.3)}$$

where ε_o is the permitivity of free space and χ is the electric susceptibility of the medium, which is related to its dielectric constant, $\varepsilon = \varepsilon_r\varepsilon_o$, and the refractive index, n_o, by

$$n_o^2 = \varepsilon/\varepsilon_o = 1 + \chi. \qquad \text{(Eq. 2.4)}$$

Once the field becomes sufficiently strong, nonlinear interactions arise within the medium and Equation 2.3 no longer adequately describes its polarization response. Externally applied optical electric fields are typically small compared to interatomic electric fields, hence the nonlinearity is usually weak and the relation between $\vec{P}$ and $\vec{E}$ deviates only slightly from the linear relation given in Equation 2.3. It is then possible to expand this definition in powers of the applied field [2]:

$$\begin{aligned} \vec{P} &= \varepsilon_o(\chi^{(1)}\vec{E} + \chi^{(2)}\vec{E}\vec{E} + \chi^{(3)}\vec{E}\vec{E}\vec{E} + \ldots) \\ \vec{P} &\equiv \vec{P}^{(1)} + \vec{P}^{(2)} + \vec{P}^{(3)} + \ldots \end{aligned} \qquad \text{(Eq. 2.5)}$$

$\chi^{(1)}$ is the same, first-order, linear susceptibility as given in Equation 2.3, and the quantities $\chi^{(2)}$ and $\chi^{(3)}$ are second- and third-order nonlinear optical susceptibilities, respectively. For simplicity, Equation 2.5 considers the fields $\vec{P}$ and $\vec{E}$ to be scalar quantities. However, for most crystalline optical materials, the nonlinear polarizability $\chi^{(n)}$ depends on the direction of propagation, the polarization of the electric field, and the orientation of the crystal. The vector properties of the electric field and polarization thus need to be considered. The optical susceptibilities $\chi^{(1)}$, $\chi^{(2)}$ and $\chi^{(3)}$ then become second, third and fourth rank tensors, respectively. If we consider an electric field incident on the medium of the form

$$\vec{E}(t) = E\cos\omega t, \qquad \text{(Eq. 2.6)}$$

and substitute into equation Equation 2.5, we get:

$$\vec{P} = \varepsilon_o\chi^{(1)}E_o\cos\omega t + \varepsilon_o\chi^{(2)}E_o^2\cos^2\omega t + \varepsilon_o\chi^{(3)}E_o^3\cos^3\omega t + \ldots$$

$$\vec{P} = \frac{1}{2}\varepsilon_o\chi^{(2)}E_o^2 + \frac{1}{2}\varepsilon_o\chi^{(2)}E_o^2\cos(2\omega t) + \frac{1}{4}\varepsilon_o\chi^{(3)}E_o^3\cos(3\omega t) + \varepsilon_o\left(\chi^{(1)} + \frac{3}{4}\chi^{(3)}E_o^2\right)E_o\cos\omega t + \ldots \quad \text{(Eq. 2.7)}$$

We can see that by allowing such nonlinear terms as given in Equation 2.5, we observe various physical processes that occur as a result of higher order polarizations $\vec{P}^{(n)}$. The first term in Equation 2.7 gives rise to a DC electric field which is called optical rectification. The second term leads to the generation of second harmonic (2ω) radiation proportional to $\chi^{(2)}E_o^2$ and the third term leads to the generation of third harmonic (3ω) radiation proportional to $\chi^{(3)}E_o^3$. The last term is the normal linear response but the linear susceptibility $\chi^{(1)}$ is augmented by $3/4\chi^{(3)}E_o^2$. Since $\chi^{(1)}$ is related to the index of refraction by Equation 2.4, Equation 2.7 describes an increase of the refractive index that is proportional to square of the electric field, E_o^2, or the intensity of the light. This is called the nonlinear refractive index or the Kerr effect (see Equation 1.1).

In optical media possessing centrosymmetry, the polarization, $\vec{P}$, must reverse exactly when the direction of the electric field is reversed, hence the second-order ($\chi^{(2)}$) term in Equation 2.7 vanishes and the dominant nonlinearity is then of third order [2]. Such materials are called Kerr media. Typically, increasing orders of susceptibility in Equation 2.7 progressively decrease by many orders of magnitude. Higher order terms may then be safely neglected. We may also neglect the third-harmonic generation process here, since it is usually weak and will not be properly phase-matched in most situations [41]. Considering

the above arguments and comparing Equations 2.7 and 2.3, we define an effective susceptibility of

$$\chi_{eff} = \chi^{(1)} + \frac{3}{4}\chi^{(3)}E_o^2 \qquad \text{(Eq. 2.8)}$$

Substituting into Equation 2.4, we obtain a new expression for the index of refraction, which now contains nonlinear terms.

$$n^2 = \varepsilon/\varepsilon_o = 1 + \chi_{eff} = 1 + \left(\chi^{(1)} + \frac{3}{4}\chi^{(3)}E_o^2\right), \qquad \text{(Eq. 2.9)}$$
$$n^2 = \varepsilon/\varepsilon_o = 1 + \chi_L + \chi_{NL}$$

where $\chi_L \equiv \chi^{(1)}$ and $\chi_{NL} \equiv \frac{3}{4}\chi^{(3)}E_o^2$ are the linear and nonlinear components of susceptibility, respectively. The polarization equation 2.5 assumes a lossless and dispersionless system. Materials which absorb light are often represented by a complex susceptibility [42]

$$\chi = \chi' + i\chi'' \qquad \text{(Eq. 2.10)}$$

while dispersive media are characterized by a frequency-dependent susceptibility, $\chi(\omega)$. For simplicity we will drop the ω term until the end. To account for losses in the system, we modify Equation 2.9 to include the absorption coefficient, α, and the complex susceptibility given in Equation 2.10 as follows:

$$\left(n - i\frac{1}{2}\alpha\frac{\lambda_o}{2\pi}\right)^2 = 1 + \chi'_L + \chi'_{NL} + i(\chi''_L + \chi''_{NL}) \qquad \text{(Eq. 2.11)}$$

where α is the attenuation coefficient and λ_o is the free space wavelength of the optical field [2]. Expanding equation 2.11 and collecting terms to lowest order we obtain

$$n^2 = 1 + \chi^{(1)\prime} + \frac{3}{4}\chi^{(3)\prime}E_o^2, \qquad \text{(Eq. 2.12)}$$

and

$$\alpha = \frac{-2\pi}{n\lambda_o}\chi^{(1)\prime\prime} - \frac{3\pi}{2n\lambda_o}\chi^{(3)\prime\prime}E_o^2. \qquad \text{(Eq. 2.13)}$$

The $\chi^{(n)\prime}$ and $\chi^{(n)\prime\prime}$ represent the real and imaginary components of susceptibility as defined by Equation 2.10. Recalling that the nonlinear index change $\Delta n = n - n_o$ is very small compared to n_o, hence $n = n_o$ and we arrive at an expression for an intensity dependent index of refraction (see Equation 1.1), $n(I)$, and absorption coefficient, $\alpha(I)$:

$$n(I) = n_o + n_2 I \qquad \text{(Eq. 2.14)}$$

and

$$\alpha(I) = \alpha_o + \beta I, \qquad \text{(Eq. 2.15)}$$

where $I = \frac{n_o c \varepsilon_o}{2} E_o^2$ is the intensity of the laser radiation, and n_o and α_o are the unperturbed linear refractive index and absorption coefficient, respectively. They are defined as follows:

$$n_o = \left(1 + \chi^{(1)\prime}_{xxxx}(-\omega, \omega, -\omega, \omega)\right)^{1/2} \qquad \text{(Eq. 2.16)}$$

$$\alpha_o = \frac{-2\pi}{n_o\lambda_o}\chi^{(1)\prime\prime}_{xxxx}(-\omega, \omega, -\omega, \omega). \qquad \text{(Eq. 2.17)}$$

The quantities n_2 and β, given by

$$n_2 = \frac{3}{4c\varepsilon_o n_o^2}\chi^{(3)\prime}_{xxxx}(-\omega, \omega, -\omega, \omega) \qquad \text{(Eq. 2.18)}$$

$$\beta = \frac{-3\pi}{c\varepsilon_o n_o^2 \lambda_o}\chi^{(3)\prime\prime}_{xxxx}(-\omega, \omega, -\omega, \omega) \qquad \text{(Eq. 2.19)}$$

are the nonlinear index of refraction and two-photon absorption coefficients.

2.2 *Physical Contributions to Third-Order Nonlinearities*

The nonlinear refractive index arises from several physical mechanisms whereby an intense electromagnetic field alters the polarization of a medium. Each mechanism typically acts on a different time scale. Consequently, the magnitude of the nonlinear response depends on the duration of the laser pulse and the mechanisms which respond on the time scale relevant to the experiment. Polarization mechanisms include the electronic Kerr response [42][41], nuclear vibrational response [41], molecular orientational response [43], and electrostriction and thermal responses [41][44][45]. The electronic Kerr response arises as a result of an increase in the atomic polarizability caused by the anharmonic deformation of the electron orbital cloud around the nucleus by the electric field of the incident light. Electronic Kerr response is not particularly large, but is of considerable importance since it is extremely fast and is present in all dielectric materials. The characteristic response time of this process can be estimated as the orbital period of the electron in its motion about the nucleus, which according to the Bohr model of the atom is found to be $\tau \approx 10^{-16} s$. The nuclear contribution arises from the dependence of the electronic polarizability on bond lengths. Induced nuclear motion modulates the bond length, hence inducing modulation of the refractive index. This contribution is related to the Raman effect and has been estimated to account for ~20% of the total non-linearity in various optical glasses [46]. The response time of the nuclear contribution is on the order of 100fs and may be observed as

"ringing" of the nonlinear refractive index on a sub-picosecond time scale [41]. This is shown in the example for 20% Nb_2O_5-80% TeO_2 glass sample in Figure 2.1.

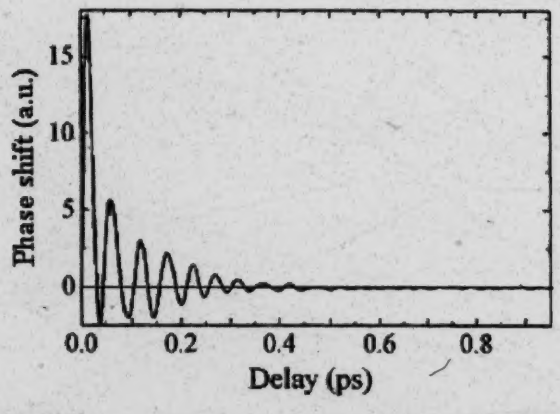

FIGURE 2.1. Nuclear response function of the 20% Nb_2O_5-80% TeO_2 glass sample obtained using a time-resolved heterodyne optical Kerr effect technique [39].

In liquids containing anisotropic molecules, the molecular orientational Kerr effect often produces the dominant contribution to the nonlinear index. The molecular axis tends to align along the applied electromagnetic field increasing the polarizability. Here, the response is dependent on the angular distribution of the molecules. The molecules cannot reorient themselves at optical frequencies since it involves displacing the full mass of the molecules instead of only the mass of the electrons. Therefore, this orientational response is slower than the electronic nonlinearity. It can be observed at a time scale of about 10^{-12}s [40]. Due to lack of freely rotatable molecules or ions, solids do not exhibit this effect.

A medium can also experience changes to the refractive index caused by mechanical strains induced by the strong electric field. This effect is known as electrostriction and its response time is roughly equal to the time required for an acoustic deformation to travel across the diameter of the optical beam or about 10^{-8}s [41][44]. Thermal effects result from refractive index changes caused by absorptive heating of the sample exposed to high-energy laser radiation. Thermal diffusion time scales are even longer, and depend on the thermal properties of the medium. Thermal nonlinearities are strong nonlinear effects, however, due to long excitation and relaxation times (usually around 10^{-6}s to 10^{-3}s and longer), this type of nonlinearity is not applicable for high-speed optical switching [41][44][45].

2.3 Resonant versus Non-Resonant Nonlinearity

In semiconductor materials, the magnitude of optical nonlinearities in the spectral vicinity of the fundamental absorption edge can become quite large owing to the optical absorption process[1]. Laser excitation creates a high density of electrons and holes, the concentration of which depends on the laser intensity. Since the refractive index of the material is dependent on the concentration of the optically generated carriers, the refractive index will then be dependent on the laser intensity. This, however, describes the $\chi^{(3)}$ process only within the general definition where $\chi^{(3)}$ is a measure of the intensity dependence of the refractive index. This process cannot contribute to third-harmonic generation and thus constitutes a different type of $\chi^{(3)}$ effect (also called dynamic or incoherent nonlinearity) [13]. At large intensities, owing to mechanisms such as phase-space filling or saturable absorption [13], the optical absorption becomes intensity dependent. The intensity dependent change in

optical absorption, $\Delta\alpha$, is related to the imaginary part of the third-order optical susceptibility, $Im(\chi^{(3)})$, which can be related to the real part of the third-order susceptibility, $Re(\chi^{(3)})$, using Kramers-Kronig relation. According to Equation 2.18, $Re(\chi^{(3)})$ describes the nonlinear index of refraction, n_2. Thus, for a material where absorption to an excited state is intensity dependent, the intensity dependent change in absorption, $\Delta\alpha$, gives rise to a change in the refractive index, Δn, by Kramers-Kronig relation [1].

In semiconductor materials, charge carriers generated at resonance typically have lifetimes in the range of tens of picoseconds, which limits the bit-by-bit switching speeds to 40 Gbits/s [47]. Resonant nonlinearities are limited to switching speeds that compete directly with electronics since they exhibit relatively slow recombination times. They are also associated with absorption, which leads to poor FOM values. Nonlinear absorption not only attenuates the signal but may also interfere with proper switching operation since it may attenuate the beam before the required nonlinear phase shift is achieved.

In the non-resonant regime, the frequency of operation falls typically below half the energy gap of the material $h\nu/E_{gap} = 0.5$. At frequencies just below the half-gap, one- and two-photon absorption processes can no longer take place, and the third order nonlinearity is purely non-resonant. As the one-third-gap is approached, however, three-photon process is resonantly enhanced and may degrade the performance. It has been shown that the best FOM is achieved when the frequency of operation falls between the half-gap and one-third-gap of the material [22]. The non-resonant nonlinearity is much smaller in magnitude compared to resonant nonlinearity, however, it exhibits an ultra-fast response time that is typically 100fs or less in glasses [22].

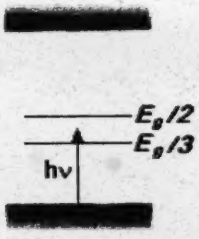

FIGURE 2.2. Frequency of operation maximizing the Kerr nonlinearity, relative to the material bandgap. The linear and nonlinear absorption is minimized by operating between the half-gap and the third-gap.

2.4 Third-Order Nonlinearities in Chalcogenide Glasses

Glasses containing heavy-metals and chalcogens (S, Se, and Te) are promising materials for non-resonant operation in nonlinear, all-optical switching applications. The easily deformable electron clouds of these atoms lead to large hyperpolarizabilities. The bandgap of these glasses can be engineered for optimal operation at the optical communication wavelength $\lambda = .1.55\mu m$. The goal in engineering a nonlinear material is large value of n_2 and a small value of β thus maximizing the FOM as given by Equation 1.3. As argued, we eliminate linear and nonlinear absorption by choosing a material to have a bandgap, E_g, slightly greater than twice the photon energy of operation. Chalcogenide glasses, however, are amorphous materials and therefore Equation 3.3do not posses a well defined band gap. They exhibit an exponential (Urbach) tail in their absorption edge, which leads to TPA even below the half-gap. In this case, the energy gap is generally defined as the point where the absorption changes from a parabolic density of states to an Urbach tail absorp-

tion. A typical value of the absorption coefficient at this point is $\alpha \equiv 1000cm^{-1}$, and this is often used as the definition of the energy gap [11][46][48]. As a consequence of the finite absorption edge, the nonlinear refractive index typically exhibits two-photon enhancement leading to large values of n_2. Of course, this increased refractive nonlinearity comes at a cost of some nonlinear absorption. Owing to the Urbach tail, the nonlinear refractive index, n_2, increases faster than TPA coefficient, β, with normalized photon energy, so the FOM exhibits a peak just below the half gap, before significant absorption takes place [48][49]. For As-S-Se glasses, the experimentally determined peak in the FOM is near $h\nu/E_{gap} \sim 0.45$ [49].

The nonlinearity of a material may be changed through the modification of either its resonant or off-resonant parts. Various researchers suggest that increasing the concentration of the highly polarizable lone electron pairs is the dominant factor in achieving large nonlinearities [48][50][51]. In the sulfo-selenide glasses, for example, progressive replacement of sulphur (S) by selenium (Se) demonstrates a monotonic increase in n_2 [49]. The polarizability of the electronic lone pairs, however, cannot be the determinative parameter here since an opposite variation has also been observed [50]. As an example, in the Ge-Se-As system, the substitution of selenium (two electronic lone pairs) by germanium (no electronic lone pairs) diminishes the nonlinear refractive index, n_2. Typically, varying the lone electron pair concentration modifies the energy gap hence it is not possible to determine whether the corresponding change in n_2 is due to lone electronic pairs or resonant, two-photon enhancement [49]. A better approximation of behavior on n_2 in chalcogenide glasses is offered by a model adopted from semiconductor two-energy-level electronic band approximation, or an anharmonic oscillator description.

2.5 *Modeling the Kerr Coefficient in As_2Se_3*

For wavelengths much longer than the two-photon absorption edge (the so-called long wavelength limit), the literature contains various formulae for approximating the optical Kerr coefficient of glasses. For example, based on a two level bond orbital model, the following approximation was proposed [22][52]:

$$n_2 = 1.7\times10^{-20}(n_o^2+2)^3(n_o^2-1)\left(\frac{d}{n_oE_S}\right)^2 \ m^2/W \qquad \text{(Eq. 2.20)}$$

where n_o is the linear refractive index in the long wavelength limit, and d is the average length of the bonds contributing to the electronic polarization (in nm). Further, E_S is the Sellmeier energy gap (in units of eV), a measure of the effective single oscillator energy. Each of n_o, d, and E_S depend to some extent on the processing history of the glass (such as the degree of structural relaxation), so there is a corresponding variability in the values reported for typical glass. As an example, for virgin (as-deposited) As_2Se_3 films, a recent study [53] gives $E_S \sim 3.86eV$ and $n_o \sim 2.67$. Using these numbers, and also assuming $d \sim 0.243nm$ [22], then $n_2 \sim 4.4\times10^{-17}m^2/W$. For well annealed films $E_S \sim 3.66eV$ and $n_o \sim 2.76$ [53], which gives (assuming no change in the average bond length) $n_2 \sim 5.8\times10^{-17}m^2/W$.

An alternative expression from Petkov and Ewen [54] (based on the well-known Boling-Glass-Owyoung (BGO) formula [55]) is:

$$n_2 = 4.1\times10^{-17}\frac{gS(n_o^2+2)^{1.5}(n_o^2-1)^2}{n_o^2E_DE_S^2}m^2/W, \qquad \text{(Eq. 2.21)}$$

where g is the anharmonicity parameter, S is an oscillator strength parameter, and E_D is the dispersion energy from the Wemple-DiDomenico model. Assuming $g \sim 1$ and $S \sim 3$ [55] and using the parameters above, plus $E_D \sim 23.74eV$ for virgin films and $E_D \sim 24.28eV$ for annealed films [53], gives $n_2 \sim 5.1\times10^{-17} m^2/W$ for virgin films and $n_2 \sim 6.6\times10^{-17} m^2/W$ for annealed films. Equations 2.20 and 2.21 are both based on a single oscillator model, and their predictions are in close agreement.

With respect to the dispersion of n_2 and β, a model originally developed by Sheik-Bahae *et al.* [56][57] has been quite successfully applied to glasses [58]. This (S-B) model determines n_2 from a Kramers-Kronig transformation of β, in turn predicted using a two parabolic band assumption. Following this approach, the frequency-dependent Kerr coefficient $n_2(\omega)$ approximates as:

$$n_2(\omega) = n_2^0 G_2(x) \qquad \text{(Eq. 2.22)}$$

where n_2^0 is the Kerr coefficient in the long wavelength (zero frequency) limit (as estimated by Equation 2.20 or 2.21, for example), and $G_2(x)$ is a function describing the dispersion of the optical Kerr effect with $x = h\nu/E_g$, the photon energy normalized to the band-gap energy. We used the analytical expression for $G_2(x)$ given as equation (39) of Reference 56. This expression predicts that n_2 should peak near $h\nu \sim 0.55E_g$ and decrease for higher photon energies, with a change of sign at $h\nu \sim 0.7E_g$. Within this model, two-photon absorption is the dominant contributor to dispersion of n_2 below the band edge. A simpler approach to modeling the dispersion of n_2 is to relate it to the dispersion of the linear index, via expressions such as Equation 2.20 and 2.21. In essence, this neglects any

contribution arising from a two-photon absorption resonance. Following this approach and using a single oscillator (S.O.) model [59]:

$$n_2(\nu) = \frac{n_o^2}{\left[1-\left(\frac{h\nu}{E_S}\right)^2\right]^4} \qquad \text{(Eq. 2.23)}$$

Expressions of this latter type are generally considered valid for photon energies well below the half-gap [52]. A family of curves can be generated using different combinations of Equations 2.20-2.23, and by assuming annealed (photo-darkened) or virgin glass. Using the aforementioned parameters for As_2Se_3 and band-gap energy of 1.79 eV (1.76 eV) for virgin (annealed) films [53], some of these curves (representing maximum and minimum predicted n_2) are plotted in Figure 2.3.

Neither of these dispersion models is expected to be completely valid. Neglecting a two-photon resonant enhancement of n_2 is in contradiction with much of the evidence in the literature [22][49]. On the other hand, the S-B model (which assumes a direct, state-free band-gap) should be considered approximate when applied to chalcogenide glasses. Because of the complex nature of their linear absorption edge, neither the direct nor indirect band-gap assumption is considered wholly correct for glasses [60]. Further, glasses have a continuum of inter-gap states and exhibit non-negligible linear absorption at photon energies well below their nominal band-gap. In particular, the level of linear and nonlinear absorption in the so-called weak absorption (Urbach) tail region probably depends on the processing history and impurity levels in the glass [22].

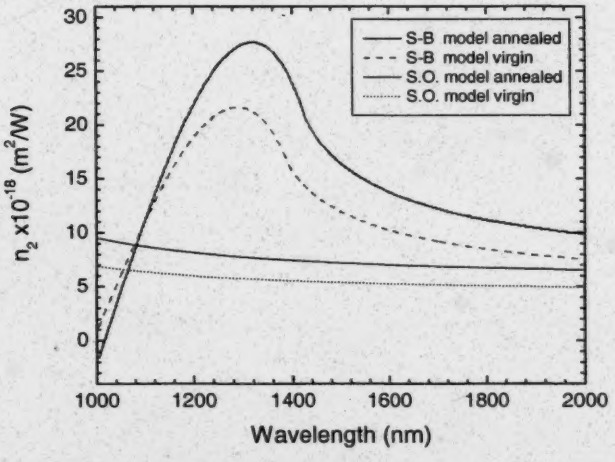

FIGURE 2.3. Theoretical prediction of spectral dependence of n_2 in As_2Se_3 glass. The upper two curves are based on the Sheik-Bahae (S-B) model (eqns. 2.21 and 2.22), and the lower two curves are based on the single oscillator (S.O.) model (eqns. 2.20 and 2.23) [61].

With regards to the TPA in glasses, there is presently no good model predicting the value of the nonlinear coefficient β, since, as mentioned, glasses do not possess a well defined bandgap owing to the presence of an Urbach tail component in the absorption which depends mainly on the composition of the glass [22].

Purifying glasses aids in "sharpening" the Urbach tail, thus minimizing the TPA and improving the FOM. Further enhancements of the already large Kerr nonlinearity of As_2Se_3, might be achieved with partial substitution of selenium by copper (Cu). This sub-

stitution results in a bandgap close to the target 1.6eV and an index of 3. Since n_2 scales as a large power of n_o in Equation 2.20, going from an index of 2.8 to 3 should increase n_2 by almost a factor of 2 [22][62]. Kerr measurements of $As_{40}Se_{55}Cu_5$ at 1.55μm, performed by J. M. Harbold *et al.* [49][62], however, revealed no increase in n_2 but an increase in TPA. The increase in nonlinear absorption can be attributed to the reduced bandgap in the $As_{40}Se_{55}Cu_5$ material, thus having a half-gap closer to the wavelength of operation. Similar results were reported with addition of tellurium (Te). Both the n_2 and the FOM are smaller in $As_{25}S_{55}Te_{20}$ than in $As_{40}Se_{60}$ [62]. Those authors concluded that the constraint on n_o and E_{gap} that arises from the need to avoid TPA limits significant further optimization of As_2Se_3 for operation at 1.55μm. In other words, As_2Se_3 is considered to be a nearly optimal glass composition for all-optical switching at fiber telecom wavelengths.

Chalcogenide glasses in the As-S-Se system simultaneously provide a large nonlinear index, n_2, and FOM that satisfies the standard criterion for all-optical switching applications. Various researchers [12][48][49][62] confirm that the nonlinearities are determined largely by the abundance of the most-polarizable constituent, selenium. As_2Se_3 has a bandgap of about 1.75eV and a large nonlinear index of about 2.8 and it is, therefore, not surprising that it produced the largest Kerr nonlinearity. The systematic increase in the linear and nonlinear index of refraction with gradual replacement of sulphur by selenium is shown in Table 2.1, as reported by J. M. Harbold *et al.* [62].

Glass	n_o @ 1.55μm	λ = 1.25μm $n_2/n_{2,As_2S_3}$	λ = 1.55μm $n_2/n_{2,As_2S_3}$
$As_{40}S_{60}$	2.45	1	1
$As_{40}S_{50}Se_{10}$	2.49	1.5	1.7
$As_{40}S_{40}Se_{20}$	2.55	1.4	1.4
$As_{40}S_{30}Se_{30}$	2.62	2.2	1.9
$As_{40}S_{20}Se_{40}$	2.70	3.5	2.1
$As_{40}S_{10}Se_{50}$	2.76	3.8	2.5
$As_{40}Se_{60}$	2.81	4.6	4.2

TABLE 2.1. Linear and nonlinear index variation with composition variation in the As-S-Se glass system as reported by J. M. Harbold *et al.* [62].

The value of n_2 typically reported for As_2S_3 is $\approx 2.0\times10^{-18} m^2/W$, which was experimentally measured using the Z-scan technique in references [63-66]. The nonlinear index and two photon absorption coefficient values for As_2Se_3, as reported by various researchers, are summarized in Table 2.2.

As_2Se_3				
n_2 (10^{-18} m^2/W)	β_2 (10^{-11} m/W)	Measurement Wavelength (nm)	Measurement Technique	Source
6.5	—	1600	Z-scan	[56]
10	0.01	1430	Z-scan	[51]
11	0.4	1500	Z-scan	[11]
18	4.5	1064	Z-scan	[50]
23	0.14	1550	SRTBC	[62]
30	2.8	1250	SRTBC	[62]

TABLE 2.2. Reported results for As_2Se_3 glass.

Along with a large value of n_2, chalcogenide glasses in the As-S-Se system also provide a FOM as large as 11 and greater [62], and are great candidates for all-optical switching applications around 1.55μm. The temporal dynamics of the third-order optical nonlinearities in As_2Se_3 will be discussed in Chapter 4.

CHAPTER 3

Differential Optical Kerr Gate Setup

The major goal of my research was to design and build a 1250nm-1600nm wavelength tunable optical Kerr gate for studying the ultrafast Kerr effect dynamics in chalcogenide glasses. Wavelength tunability in the 1250nm-1600nm region was attained with the use of an optical parametric amplifier (OPA), pumped by a Ti:sapphire laser amplifier generating 800nm, 100fs pulses at a repetition rate of 1kHz. The pulse duration at the output of the OPA is slightly shorter than the pulse duration of the pump laser (<100fs). The differential optical kerr effect (DOKE) detection technique was originally described in reference [27] and built for single wavelength operation at 800nm. The broad wavelength range targeted in the present work poses an added difficulty to the setup since it places constraints on all its optical components. Each component must perform its expected function in the

entire 1250nm - 1600nm wavelength range without the need for readjustments. This includes wave-plates, polarizers, beam splitters, lenses, mirrors and photodetectors. With this in mind, achromatic half- and quarter-wave plates were employed, giving the same $\lambda/2$ and $\lambda/4$ wave retardation, over the 1200nm - 1600nm range. Lenses, polarizer prisms, and beam splitters and samplers are coated with broadband (1050-1620nm) anti-reflection (BBAR) coating. For signal detection, the photodetectors employ large-area (3mm diameter) InGaAs photodiodes.

3.1 Overview of the DOKE System

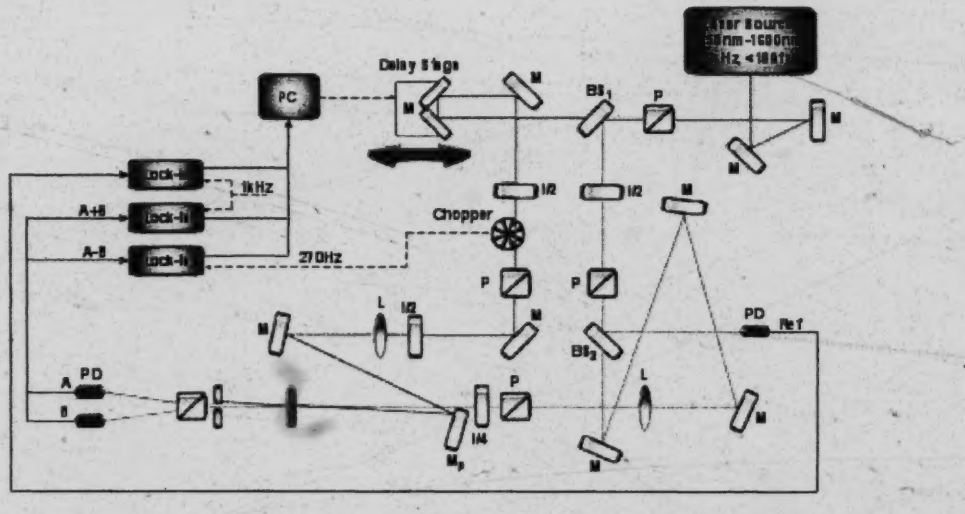

FIGURE 3.1. Schematic diagram of the differential optical Kerr effect (DOKE) experimental setup

Figure 3.1 illustrates the main components of the DOKE setup. At the output of the OPA, the OPA signal and pump beams are separated using a polarizer (not shown in figure), as the two beams are polarized orthogonally to each other. Remaining fluorescence and idler signals are filtered using a 1200nm -1650nm band pass filter (not shown in figure). This can also be done using a simple aperture, since the stray and signal beams are not collinear. Using a 50/50 beamsplitter, the vertically polarized beam is split into two beams, one for the pump and one for the probe. One side of the beamsplitter is BBAR coated to prevent double reflections of the beam. The pump beam then travels through a retro-reflector mounted on a computer controlled time-delay stage. The delay stage can be precisely controlled with a 0.7fs step resolution giving more than enough precision for performing sub-picosecond time resolved scans. Both the probe and the pump beam travel through a half-waveplate/polarizer pair which is used for beam intensity control. As the linearly polarized beam passes through the half-wave plate, its polarization is rotated by an amount 2θ, where θ is the angle that the fast axis of the waveplate makes with the vertical polarization of the beam. The polarizer then rejects the horizontal component of the polarization, effectively attenuating the beam and restoring its original, vertical polarization. Keeping the polarizer fixed, the waveplate may now be rotated between $\theta = 0°$ and $\theta = 45°$ to give a maximum to zero transmission variation at the output of the polarizer. The achromatic wave-plates, however, do not perform ideally and leak enough of the original beam polarization to severely degrade the transmitted signal, making it unusable. This is easily fixed by placing the polarizer perpendicular to the beam's original polarization. Any leakage through the wave plate is then blocked, and the beams may now be attenuated to ~0. With this arrangement, the light transmission at maximum attenuation is cut down from ~2% to ~0.1%, significantly improving the extinction ratio.

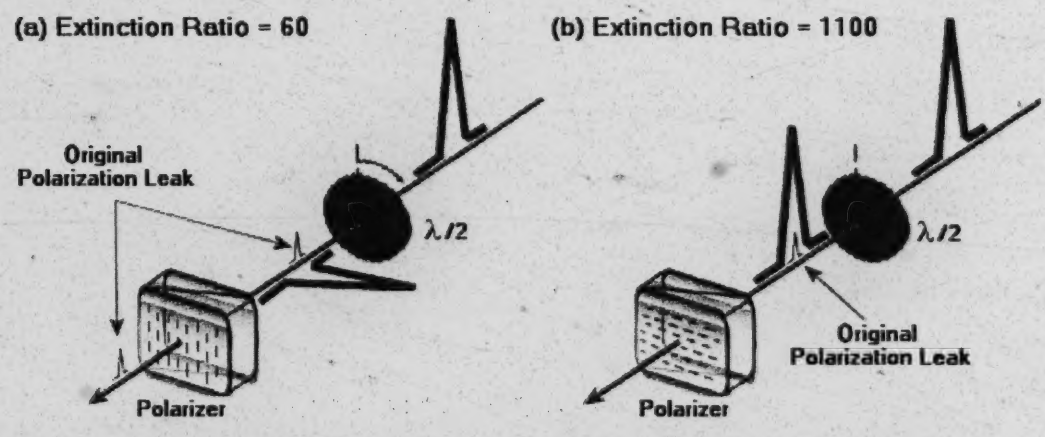

FIGURE 3.2. Schematic diagram of the beam attenuator. Unwanted leakage of the original polarization passes through the polarizer thus degrades our signal (a). This leakage signal is blocked by crossing the polarizer with the original polarization (b). Rotating the half-wave plate between θ=0° and θ=45° gives us the full range of intensity control.

After travelling through a variable delay arm, the probe beam is then circularly polarized and focused onto the sample. The variable delay arm is a three mirror setup compensating for the mismatch of the distance travelled between the pump and probe beams from the first beamsplitter. It is used for an initial, rough temporal alignment of the pump and probe signals. Fine temporal alignment was performed before each experiment using the computer-controlled delay stage. After travelling through the delay arm, the probe beam passes through a quarter-wave-plate, which is oriented to produce a circularly polarized probe beam at its output. Proper circular polarization is ensured by sending the beam back through the quarter-wave-plate/polarizer pair, and adjusting the orientation of the wave-plate while monitoring the intensity of the return beam. A circularly polarized beam reflected back through the quarter-wave-plate becomes linearly polarized and perpendicu-

lar to the its original polarization. Hence it will be blocked by the polarizer. Adjusting the waveplate until the return signal is completely extinguished, consequently indicates circularly polarized forward beam.

Post-sample, the probe beam travels through a Wollaston prism where the horizontal and vertical polarization components are separated and detected with a pair of photodetectors A and B. The photodetector output signals "A-B" and "A+B" are then detected separately by a pair of lock-in amplifiers. A third lock-in amplifier is used to detect the probe beam at 1kHz, sampled with a beamsampler BS_2, placed just before the delay arm. This provides a pre-sample beam reference and also serves as an important laser diagnostic and monitoring tool. Although the A+B signal acts as our main probe beam detector, since it provides us information regarding the post-sample probe intensity, the comparison between A+B and the probe reference detector alerts us of sample-related problems such as reflection scatter and absorption.

The pump beam is chopped by a 50% duty cycle optical chopper at 270Hz. Using a half-wave plate, it is polarized at 45° to the fast axis of the analyzer, and also focused onto the sample. The pump beam is directed at the sample with the pick-off mirror M_p, which is brought to a close proximity with the probe signal path. Reflecting the pump off the edge of the mirror allows the pump and probe beams to be nearly colinear. The pump and probe focusing lenses are chosen so that the probe beam focuses tighter on the sample than the pump beam. The chosen focal lengths of the lenses were *400mm* and *250mm* for pump and probe beam focusing, respectively. This ensures that the probe beam fits well within the spot diameter of the pump, and also reduces the detected Kerr signal noise caused by spa-

tial jitter of the beams. For pump beam monitoring and diagnostics, a beam sampler is placed in similar fashion to the probe beam sampler (not shown in the diagram).

As discussed in Chapter 1, when a strong pump beam passes through the sample it induces a local birefringence, which in turn rotates the polarization of the probe pulse from circular to elliptical. This rotation can then be easily seen as a difference in the detected A and B signals. Using an optical chopper synchronized with the laser output, we modulate the pump beam at a frequency of 270Hz, which results in modulation of the probe signals A and B. The modulation depth of the detected probe beams represent the magnitude of the Kerr effect in a given sample as long as the probe beam is not strong enough to itself induce any Kerr effect in the sample. Having the pump beam polarized at 45° to the fast axis of the analyzer prism allows maximum modulation of the "A" and "B" signals of the probe, as detected by the differential detector. In other words, this gives the maximum detected "A-B" Kerr signal. The differential signal vanishes with pump beam polarization at 0°, and the detected signal provides an independent information of the sample's nonlinear absorption, β.

3.2 DOKE Formulations

The pump beam polarized at 45° incident on the sample induces a birefringence of $\delta\phi = \phi' + i\phi''$, where ϕ' and ϕ'' are the real and imaginary components of the phase retardation, respectively. This phase shift is given by

$$\phi' = 2\pi\frac{n_2 d}{\lambda} I_{pump}, \text{ and} \quad \text{(Eq. 3.1)}$$

$$\phi'' = d\beta I_{pump} \quad \text{(Eq. 3.2)}$$

where d is the thickness of the sample, and I_{pump} is the pump beam intensity. The "A+B" and the "A-B" signals of the circularly polarized probe signal passing through the sample are then detected by the differential photodetector. Taking the ratio of the detected signals gives us the following relationship [27]:

$$\frac{A-B}{A+B} = \frac{\sin\phi'}{\cosh\phi''} \quad \text{(Eq. 3.3)}$$

With the pump beam polarized at 0°, the detected signal ratio is given by [27]

$$\frac{A-B}{A+B} = \tanh\phi''. \quad \text{(Eq. 3.4)}$$

Alternating between the two pump polarization conditions (45° and 0°), the ϕ' and ϕ'' terms can be separated, yielding the real and imaginary components of $\chi^{(3)}$, or the nonlinear index of refraction, n_2, and absorption coefficient, β, respectively. In the absence of large nonlinear absorption, as in chalcogenide glasses where β is usually very small at the wavelength of interest, $\phi'' \approx 0$. The Equation 3.3, in this case, simplifies to

$$\frac{A-B}{A+B} = \sin\phi'. \quad \text{(Eq. 3.5)}$$

The complete derivation of the given equations, as originally demonstrated in reference 27, is given in Appendix A.

3.3 DOKE Detection System

Large-area (3*mm* diameter) InGaAs photodiodes, with sensitivity in the *1100nm - 1650nm* range, are employed for signal detection in the DOKE setup. Those do not need to be fast photodiodes. The detection system only needs to be able to detect relative intensities of pulses arriving at a frequency of 1kHz. In fact, the detection system should provide electrical pulses with a time constant long enough for performing accurate measurements by the lock-in amplifiers, but short enough so that the response dies out completely before the arrival of the next pulse. With the computer controlled delay stage, we are able to set a specific time delay between the pump and the probe pulses and remain at that delay setting as long as needed. For each delay setting, the photodetectors are then able to collect hundreds of probe pulses, which are then averaged by the lock-in amplifiers. The averaged photodetector signals for each time delay stage setting, collected by a PC, consequently yield a time resolved Kerr profile of the sample under test. With this in mind, the detection system is designed as described below.

3.3.1 Photodetectors

The chosen photodiodes require a circuit that contains a current-to-voltage converting element such as resistor (passive) or transimpedance operational amplifier (active). In addition, the photodiodes may be operated in the photovoltaic unbiased mode, or photoconductive mode in which a reverse bias is applied across the photodiode. Out of these choices, photoconductive mode with active external circuit offers the best response linearity at a small cost of circuit complexity [67].

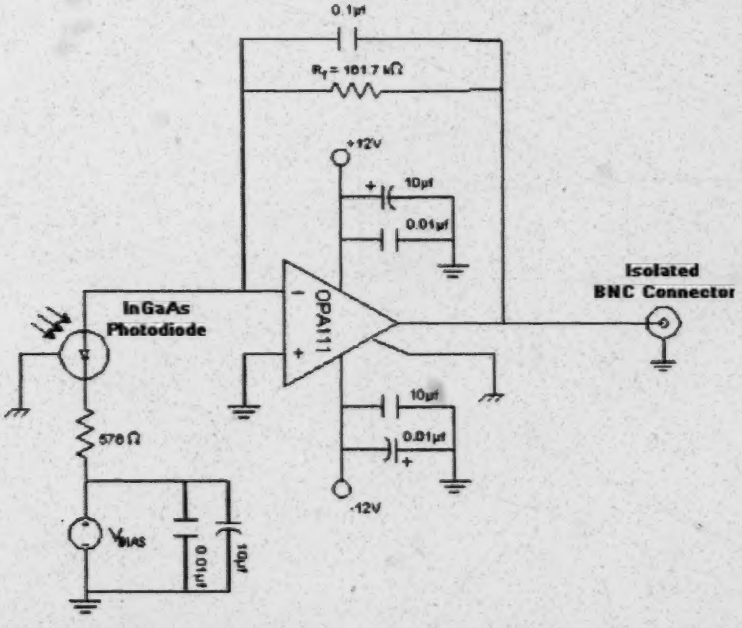

FIGURE 3.3. Photodetector circuit schematic utilizing a low noise transimpedance amplifier in a photoconductive mode.

Figure 3.3 shows the photodetector circuit. A 0.01µf ceramic capacitor and 10µf tantalum capacitor are used to clean up any potential input power noise. To limit the maximum current through the photodiode (*20mA maximum*), a 576Ω resistor is placed in series. The supply, V_{bias}, provides 1.8V reverse bias for the photodiode. The feedback resistor, R_f, sets the gain of the amplifier circuit.

$$V_o = (I_p + I_b)R_f \quad (V), \qquad \text{(Eq. 3.6)}$$

where I_p is the photocurrent and I_b is the amplifier biasing current. Using low noise, Burr-Brown, OPA 111 operational amplifiers, the maximum bias current of 5pA is small compared to the photocurrent values and can be neglected in the gain calculation. With photodiode responsivity around 0.9A/W, the output voltage of the detection circuit is

$$V_o = 0.9R_f \cdot P_{Laser} \ (V), \qquad \text{(Eq. 3.7)}$$

where P_{Laser} is the detected laser power. A 162KΩ resistor was chosen for the feedback resistor R_f. With typical detected laser power around 25μW for example, this gives an output voltage of approximately 3.5V for the detection circuit. This voltage is too large to detect with the Lock-in amplifiers used, which have a maximum range of 0-500mV. However, choosing a smaller value (between *10* and *100 KΩ*) for R_f would make the detection circuit response nonlinear since the smaller resistance puts too much load on the photodiode and its biasing circuit. To overcome this problem, a piece of diffuse glass was placed in front of each photodiode in order to attenuate the incoming laser power. This lowered the output voltage of the detection circuit to levels that can be easily handled by the lock-in amplifiers. A capacitor in the feedback loop is used as an integrator. It is used in parallel with the feedback resistor in order to "smooth out" the ringing in the detector response. The capacitor value is chosen so that the response decays completely before the arrival of next laser pulse. With 1nf capacitor and laser pulses ~1ms apart (1kHz laser repetition rate), this gives about 6 time constants between two consecutive laser pulses. This is adequate for the response to die out sufficiently before the arrival of the next laser pulse.

The same circuit was constructed for the detection of pre-sample pump and probe reference signals as well as the post sample probe signals “A” and “B”. In the post sample

detection system, we are actually more interested in obtaining the "A+B" and "A-B" response signals rather than individual "A" and "B" signals. Consequently, unity gain summing and difference amplifiers were integrated into the post-sample detection system. This provides the "A+B" and "A-B" signals. The summing and difference amplifiers are shown in Figure 3.4 .

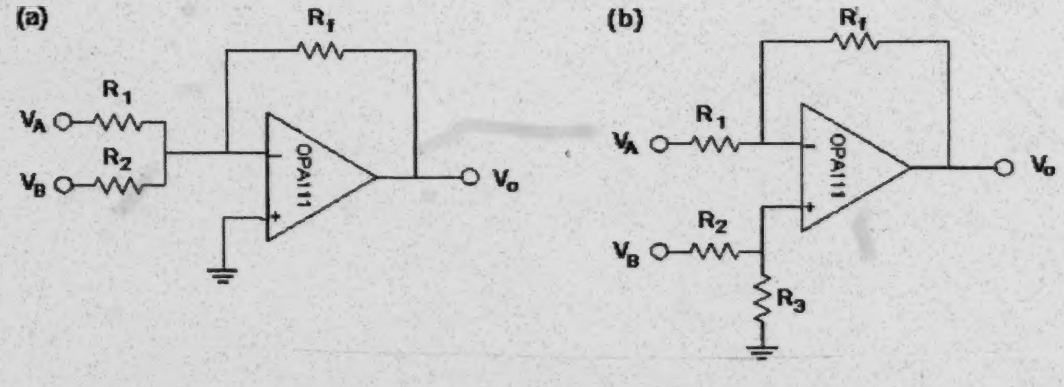

FIGURE 3.4. Schematic diagram of (a) summing amplifier and (b) difference amplifier.

The output of a summing amplifier is given by:

$$V_o = -R_f\left[\frac{V_A}{R_1} + \frac{V_B}{R_2}\right] \ (V). \qquad \text{(Eq. 3.8)}$$

With $R_f = R_1 = R_2$, Equation 3.8 becomes

$$V_o = -(V_A + V_B) \ (V), \qquad \text{(Eq. 3.9)}$$

giving the desired summation of the signals, "A+B". Resistance value of 10kΩ was chosen for resistors R_f, R_1 and R_2. This yields load currents in the μA-mA regime which the transimpedance amplifier in the previous stage can easily provide. The minus sign in the equation indicates that the output will be inverted. This makes no difference to the lock-in amplifiers, hence an inverting circuit is not necessary.

Similarly for the difference amplifier, the governing equation for the output is given by

$$V_o = -\left[\frac{R_f}{R_1}\right]V_A + \left[1 + \frac{R_f}{R_1}\right]\left[\frac{R_3}{R_2 + R_3}\right]V_B \quad (V). \qquad \text{(Eq. 3.10)}$$

Again, with $R_f = R_1 = R_2 = R_3$ Equation 3.10 reduces to

$$V_o = V_B - V_A \quad (V), \qquad \text{(Eq. 3.11)}$$

and thus the desired difference operation, "A-B" is obtained. The complete circuit diagram of the differential detection system is shown in Figure 3.5.

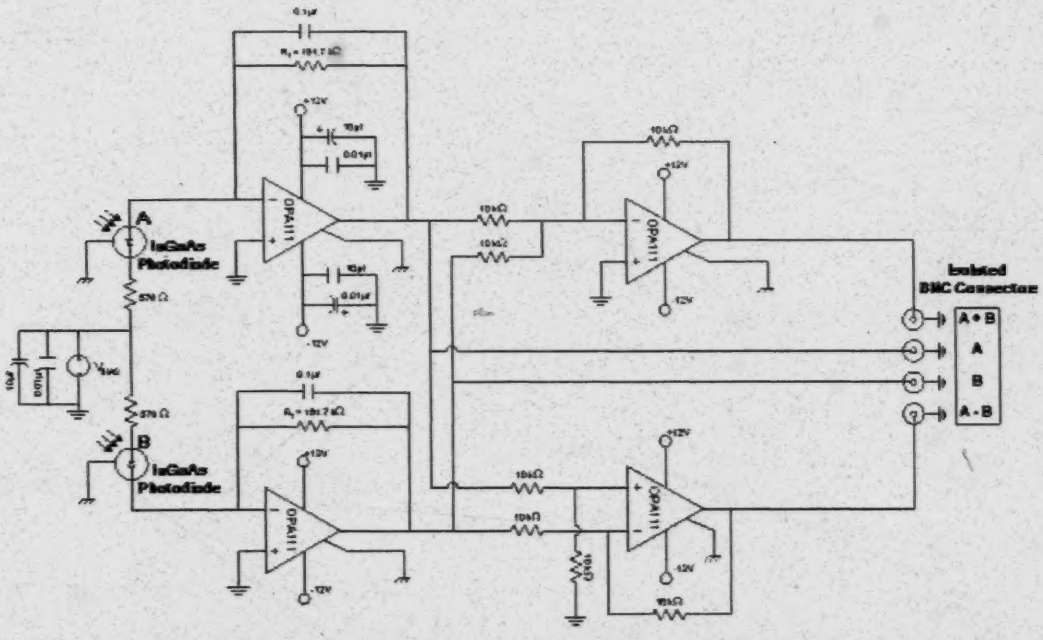

FIGURE 3.5. Circuit diagram of the differential detection system employing two transimpedance amplifiers (one for each signal A and B), and unity gain summing and difference amplifiers.

The photodiode bias voltage, V_{bias}, and the power supply for the amplifiers was provided by an external power supply.

3.3.2 Power Supply

To power the detection circuits, a clean, linear, triple output, Power-One power supply was chosen. It was able to provide minimal noise power for the detection circuit. The detection circuit power supply was configured as demonstrated in Figure 3.6. The three outputs of

the Power-One power supply include ±12V, for energizing the operational amplifiers of the detection circuit, and +5V, for biasing the photodiodes. Since maximum reverse bias voltage for the chosen photodiodes is 2V, the 5V output is connected to a 1.8V voltage regulator to provide appropriate bias voltage for the photodiodes. The power to the photo-detector circuit is delivered via a 4-wire (*±12, +1.8, GND*) shielded cable.

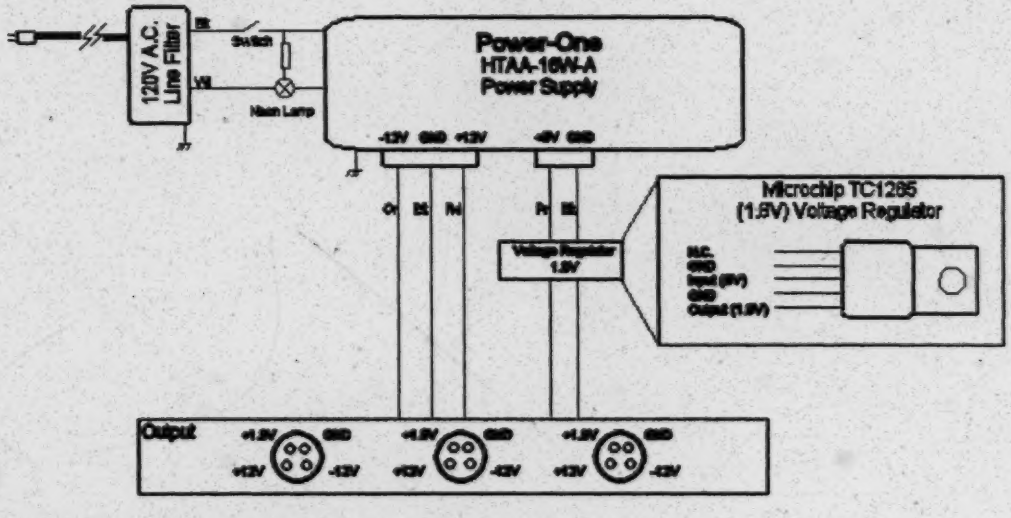

FIGURE 3.6. Diagram of the power supply for the detection circuit.

The calibration and characterization of the detection system are described in the following section.

3.4 Photodetector Characterization and Calibration

The next step was to calibrate the detectors and, most importantly, test them for linearity. In order to do this, the photodetectors were mounted in the setup as shown in Figure 3.1. The probe reference photodiode and the differential detector signals "A" and "B" are connected to separate lock-in amplifiers connected to a PC. While varying the laser intensity between $\sim 0\mu W$ and $\sim 800\mu W$, 500 data points was collected at 900ms intervals for each of the photodetectors. Since the detected signals will typically be $< 250\mu W$, this provided adequate dynamic range to assess the linearity of the detectors. To check for linearity, the data from each photodetector were plotted against the data from the other. Figure 3.7 shows the response of each photodetector plotted against the response of the other along with the corresponding linear fit.

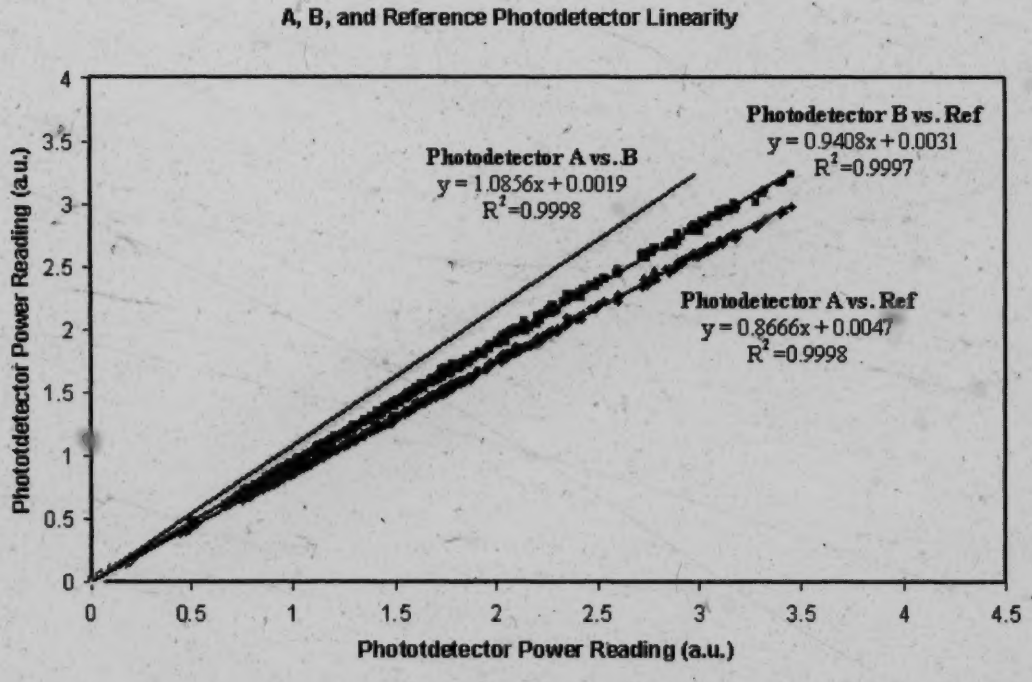

FIGURE 3.7. Plot of the photodetector response to varying laser intensity. We plotted the response of photodetector "A" vs. "B", "A" vs. "Ref" and "B" vs. "Ref" to verify linear response. Each plot is fitted to a line.

With linear regression $R^2 = 0.9997$, each photodetector shows an excellent relative linear response. To ensure that the detectors are not just linear to each other, one of the detectors was replaced with a Newport power meter that was known to be linear, and the experiment was repeated. Figure 3.8 shows the obtained results.

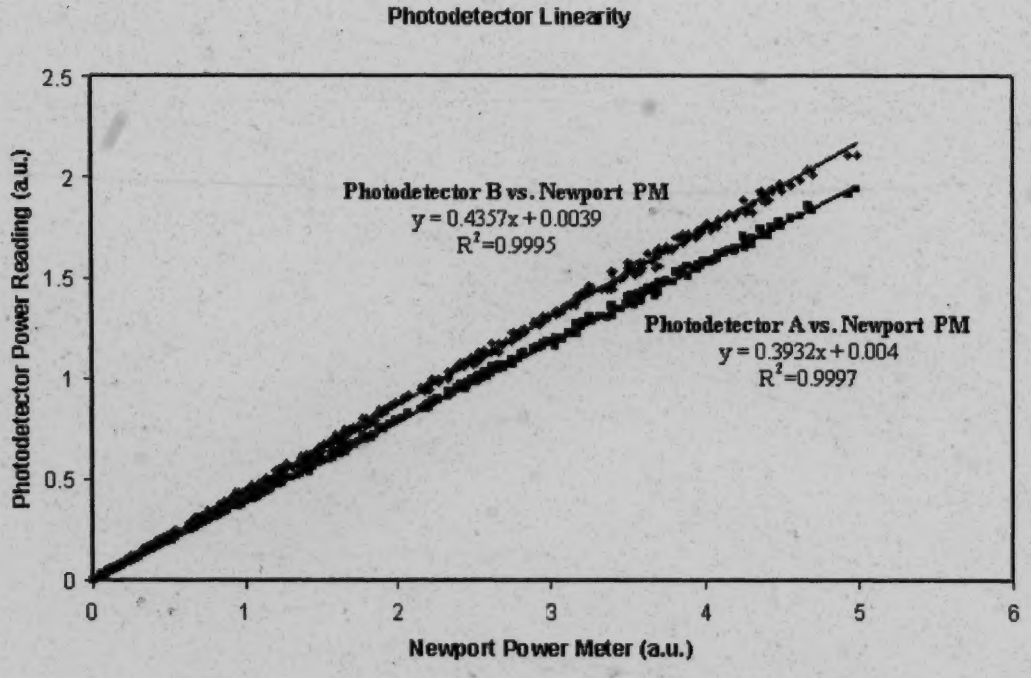

FIGURE 3.8. Plot of the photodetector response to varying laser intensity. Plotted is the response of photodetector "A" and "B" vs. a Newport power meter. To demonstrate linear response, each plot is again fitted to a line.

Note the small, non-zero y-intercept value on each of the curves. This means that there is a small offset voltage present due to background noise when no light impinges on the detectors. This value is small enough that it will not significantly impact the accuracy in our system. Also note that each of the plots has a different slope. This indicates that each photodetector exhibits slightly different responsivity and will require a separate calibration

curve. Most importantly, all of the photodetectors show a highly linear response in the range of interest. Although the detectors are calibrated using a power meter before each experiment, absolute power measurements are not necessary. All of the measurements involve measuring only relative intensities. To measure the Kerr signal we only measure the modulation of the probe signals "A" and "B", hence absolute power measurement is not required. In this case, it is only necessary to ensure proper operation of the difference amplifier; i.e. it is necessary to ensure the "A-B" output gives the same result as the difference between the individual signals, "A" - "B". To test this, we monitored the differential detector output signals "A", "B" and "A-B", as the polarization of the probe signal is varied from circular to elliptical, thus modulating the "A" and "B" signals. 250 data points were collected in this manner and the results are plotted in Figure 3.9, which shows the "A-B" signal versus the difference of the individual signals, "A"-"B".

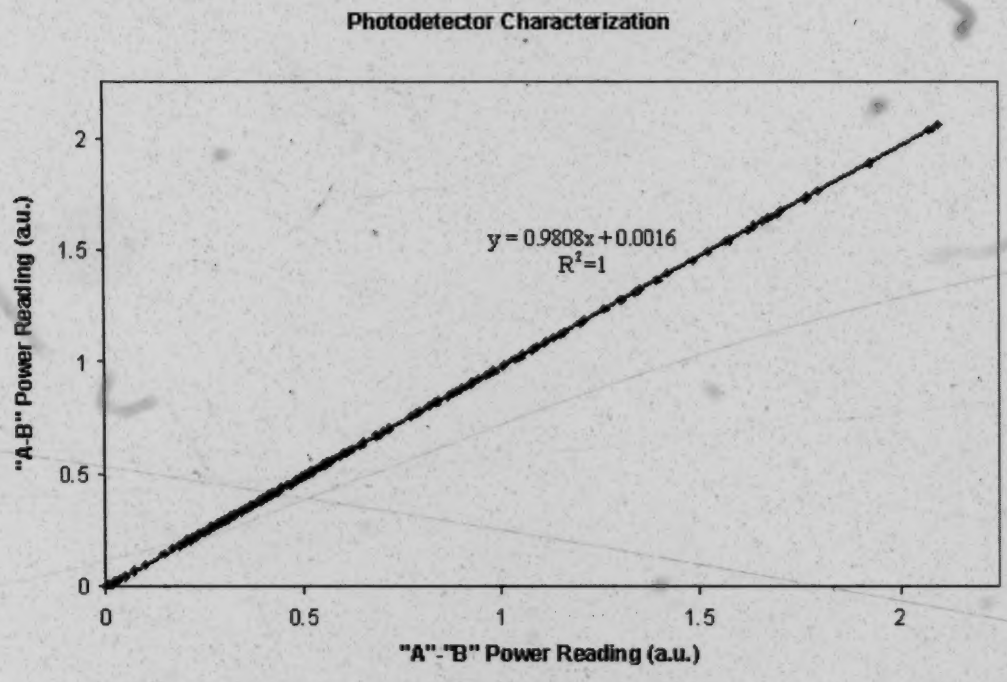

FIGURE 3.9. Differential photodetector. Plot of signals "A-B" vs. "A"-"B"

Since the two signals follow each other very closely and with the slope very close to 1, we concluded that the difference amplifier operates as expected and the signal did not require any further calibration. This was not the case in Reference 27, where a calibration constant was required to calibrate the system to give "A" - "B" equal to "A-B"

Although an accurate, absolute measurement of the pump beam intensity is typically needed for Kerr measurement, a photodetector sampling the pump beam in our setup is not necessary. Any fluctuations of the pump beam caused by the laser source can be observed in the behavior of the probe beam. Since both pump and probe signals come from the same laser beam, their respective behaviors will be almost identical. This is illustrated in Figure 3.10, which shows the simultaneous behavior of the sampled pump and probe beams with varying intensity.

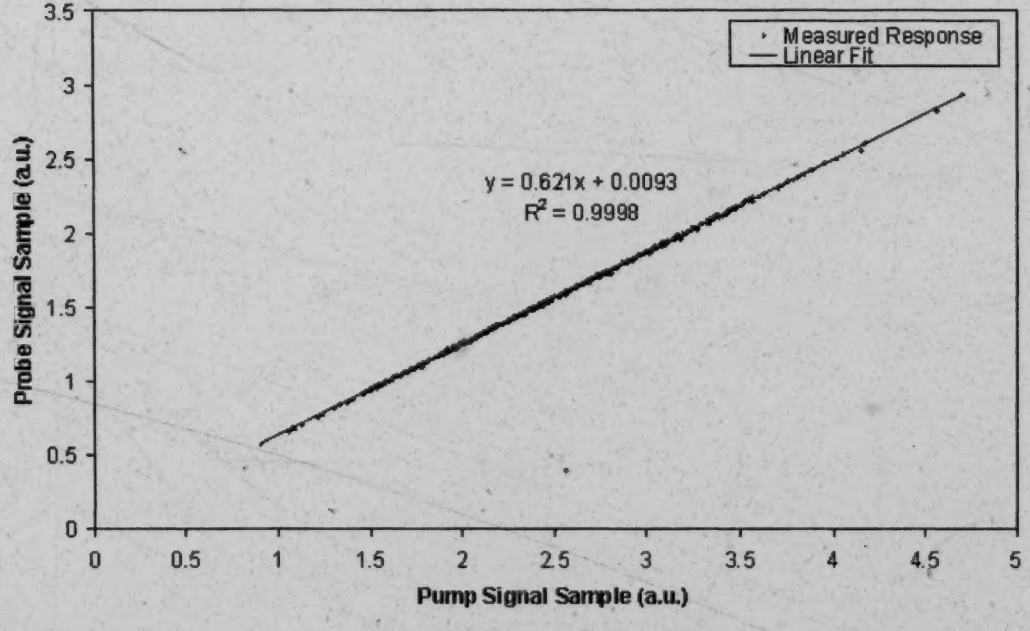

FIGURE 3.10. Relation between the pump and the probe signal references.

As can be seen by the linear fit, the intensity fluctuations of the beams follow each other very closely. We could, therefore, measure the absolute power of the pump beam only at the beginning of the day, or after attenuator adjustment, and monitor its power fluctuations with the probe reference photodetector throughout the subsequent experiments. This eliminated the need for pump beam sampling during an experiment.

In the setup, the reference photodetector has another very important role, which is signal noise reduction. The laser light at the output of the OPA comes from a second order parametric process which is highly sensitive to the pulse profile and intensity fluctuations of the pump laser. Any fluctuations of the OPA pump beam are greatly amplified at its output. The resulting beam is, consequently, quite noisy. It tends to drift spatially and fluctuate in intensity. This introduces noise in the detected Kerr signal through intensity fluctuations of the probe signal, the pump signal, as well as fluctuations in spatial overlap of the pump and probe beams at the sample. The latter effect is significantly cleaned up by the focusing lenses. The detected Kerr signal is also insensitive to the intensity fluctuations of the probe beam owing to the post-sample reference detector "A+B". This includes rapid fluctuations as well as long period laser drifts of the probe signal. Much of this noise is cleaned up by dividing the "A-B" Kerr signal by the "A+B" probe signal in the nonlinear phaseshift calculation, ϕ_{NL}, as per Equation 3.3. Dividing again by the normalized reference signal cleans up some of the remaining noise coming from the rapid intensity fluctuations in the pump beam. Slow intensity drifts in the pump beam do not pose a problem in the setup. The pump beam intensity is monitored throughout each experiment and a corresponding value is then used in the calculations. Figure 3.11 demonstrates typical rel-

ative intensity fluctuations of the OPA laser beam, which cleans up significantly with the use of pre-sample reference detector.

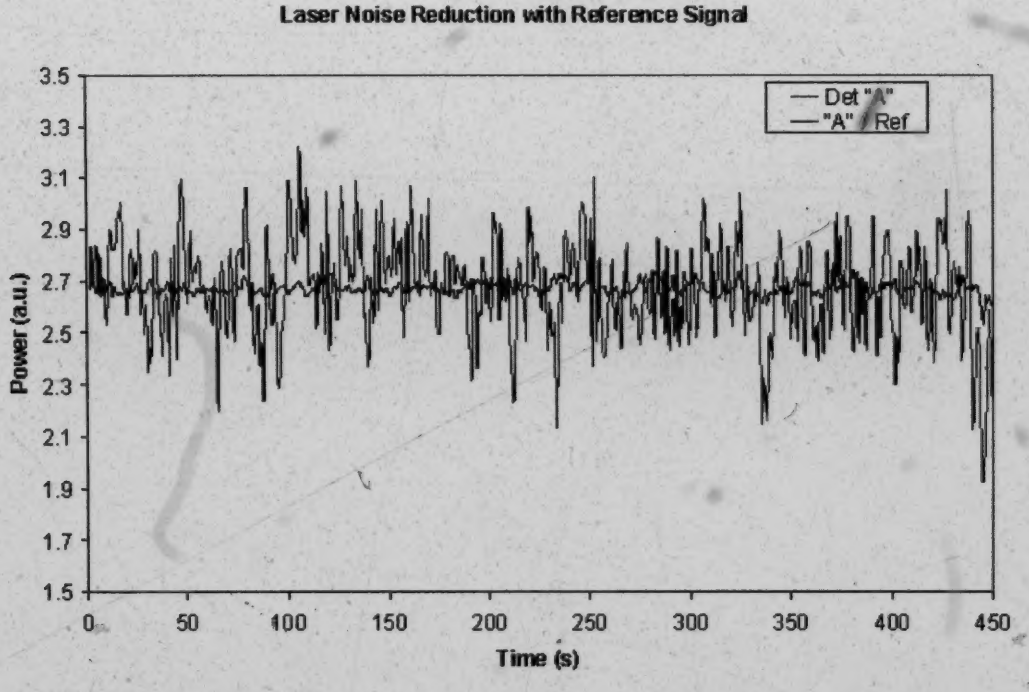

FIGURE 3.11. OPA laser intensity fluctuates by as much as 20% in this case. Much of this noise can be eliminated with the use of a reference detector.

3.5 *Temporal Alignment of the Pump and Probe Beams*

The first step to finding a Kerr signal is to locate the exact position of the computer controlled stage, where the pump and probe pulses are overlapped in time. With Kerr signals as short as the duration of the pulse ($\approx 100fs$), the signal may be observed over a range of stage position spanning only 0.03mm. The general stage position for zero pump delay time did not change from day to day; however, small adjustments were necessary on a daily basis or after each laser realignment. A simple procedure for finding the zero pump delay time involves using a thin piece of a β-BBO crystal on a rotating mount. Keeping the intensity of the pump and probe signals at maximum for best visibility, the two beams were first spatially aligned. A pinhole aperture was placed in the sample holder and its position was adjusted until the pump beam was fully visible with an IR viewer, on a screen placed behind the aperture. Next, the pump mirror M_p was adjusted until the pump beam was also visible on the screen. Once the spots were roughly spatially aligned, the aperture was replaced with the rotating mount holding the β-BBO crystal. Passing through the crystal, the pump and probe beams were frequency doubled and two visible red spots appeared on the screen. Adjusting the angle of the crystal and observing the intensity of the red, (2ω), spots, we searched for a position of maximum efficiency for second harmonic generation. At this point, the timing of the pump pulse was varied with respect to the probe pulse by slowly moving the stage. When the two beams became aligned in time, a third red spot emerged at an angle bisecting the pump and probe beams. The temporal alignment was maximized with fine adjustments of the stage until the middle spot appeared the brightest [27].

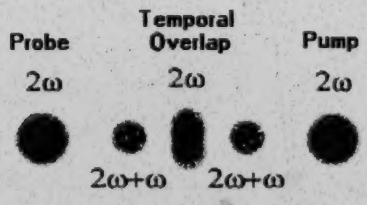

FIGURE 3.12. Visible spot pattern through β-BBO crystal at zero pump-probe time delay. When the pulses are not aligned in time, only the two outer spots are present.

With good temporal alignment and enough laser intensity, two more spots become clearly visible on the screen. The two blue spots on either side of the centre spot, as indicated in Figure 3.12, represent third harmonic of the original signal created by mixing of the first and second harmonic signals ($3\omega = 2\omega + \omega$). The setup was then ready for Kerr characterization and experiments.

CHAPTER 4

Setup Characterization and Results

With the properly functioning detection system established in Chapter 3, we next proceeded with the characterization of the Kerr gate setup. Becoming familiar with the intricacies of the DOKE system occupied a large portion of the research process. Before we could proceed with testing of actual samples, a number of diagnostics such as the verification of the correct beam intensity, determination of spot sizes and beam autocorrelation were necessary. We cannot hope to describe all of the diagnostic tests that were performed throughout this research project. We do, however, discuss the diagnostics crucial to the working of the DOKE setup. Furthermore, to verify the accuracy of our results, we performed various tests using samples of fused silica and a carbon disulfide [CS_2], the results of which may then be easily verified with their well known and documented characteristics

in the literature. Finally, with the properly functioning optical Kerr gate, we proceeded with studying the Kerr dynamics of chalcogenide glass films.

4.1 Beam Diagnostics

It was necessary to assess pulse duration and the spatial beam profile characteristics at the sample, as they impact the quality of the Kerr signal. They are also necessary parameters in the accurate determination of the $\chi^{(3)}$ values.

4.1.1 Spatial Beam Profile

The spatial beam profile describes the transverse intensity profile of the beam. Ideally, this profile is Gaussian. However, any degradation or dispersion in the beam, caused by the laser source or non-ideal optics, will lead to a non-Gaussian profile. This is especially true in our case where, with the use of the OPA, the pulses were not perfectly Gaussian. In any case, a perfectly Gaussian pulse is not crucial for proper operation of the Kerr gate, so long as it is roughly symmetric with a flat or rounded peak.

To measure the spatial profile of the beam we placed a photodetector behind a 20μm pin-hole and mounted it in the sample holder. We connected the photodetector to the lock-in amplifier and then to PC for data acquisition. With the sample micrometer (μm) stage we centered the pump beam on the pinhole by maximizing the photodetector power readout. Having properly centered the beam on the pinhole, we then used the μm-stage to scan the pinhole in the transverse plane of the beam along the z-direction, while recording power measurements. For each micrometer position we collected and averaged 50 data points at

300ms intervals. Next, to verify that the beam was roughly circular, we re-centered the beam on the pinhole and repeated the measurement along the y-direction. This process was repeated for the probe beam. The results are shown in Figure 4.1.

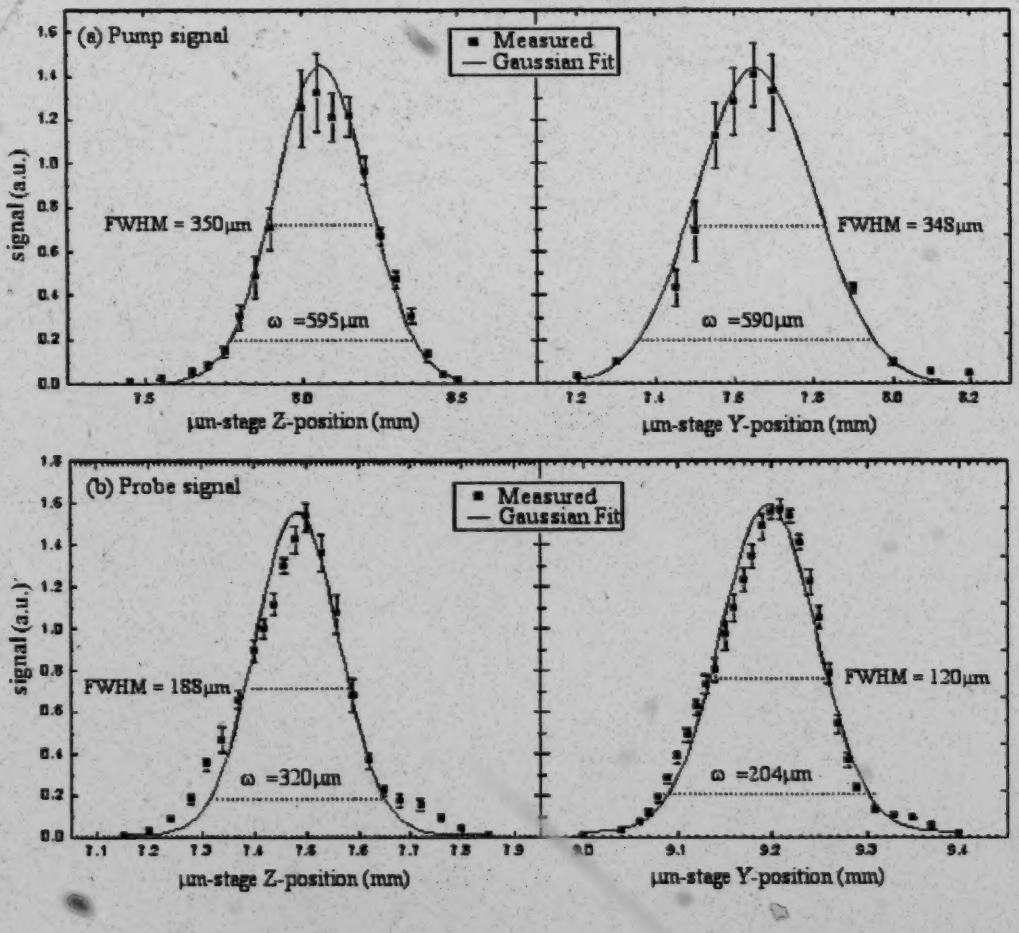

FIGURE 4.1. Spatial profile of (a) the pump and (b) the probe beams. The pump beam is circular with a spot size of about 590μm. The probe beam is elongated in one direction with beam waists $\omega_1 = 320\mu m$ and $\omega_2 = 204\mu m$.

Traditionally, the waist, ω_o, of a gaussian beam is defined as the full width between $1/e^2$ points of the peak intensity. We use this definition to define the spot diameter of our pump and probe beams. The pump beam is circular with a beam waist $\omega_o \approx 590\mu m$. The probe beam is much smaller as expected. With a beam waist $\omega_o \leq 320\mu m$, the probe beam fits well within the diameter of the pump beam.

Moving away from the focus, the beam starts to diverge and has larger diameter than the value determined at the focus. Hence, it was also useful to estimate the depth of focus, to ensure approximately uniform beam intensity throughout the thickness of the sample. If we define the depth of focus as the distance between two points along the beam where the beam is $\sqrt{2}$ times larger than it is at the beam waist, we can determine the depth of focus for a system employing a gaussian beam [27]:

$$DOF = \left(\frac{8\lambda}{\pi}\right)\left(\frac{F}{D}\right)^2 \qquad \text{(Eq. 4.1)}$$

If we focus the probe beam with a 250mm focal length lens, and the beam diameter is roughly 2-3μm, then the depth of focus for the beam is about 2.5cm. This value is even larger for the 500mm focal length lens used to focus the pump beam on the sample. With sample thicknesses no lager than 2mm, it is safe to assume that the beam diameter, hence the intensity, was uniform throughout the sample thickness.

4.1.2 Beam Autocorrelation

The pulses' autocorrelation determines the resolution and the shape of the Kerr scan, and is also crucial in the calculation of the laser beam intensity. Very fast nonlinear effects, such as the electronic polarizabilities, follow the intensity envelope of the pump pulse resulting in a Kerr scan which provides a perfect autocorrelation of the pulse. A Kerr scan involving non-instantaneous and longer lasting effects will result in a profile showing the convolution of the response function and the temporal profile of the pump pulse. Since fused silica [SiO_2] glass possesses a Kerr response which is purely electronic, it can be used to obtain an in-situ autocorrelation. Figure 4.2 shows the pulse autocorrelation of the beam at the sample position. We obtained this by first overlapping the pump and probe beams in space and time at the sample. We then placed a sample of fused silica in the sample holder and with fine adjustments of the sample stage and the mirror M_p, we maximized the "A-B" output, i.e. the Kerr signal. During this experiment, we ensured that the pump beam is polarized at 45° to the analyzer. With fine adjustments of the pump beam half-waveplate, we again looked for a maximum Kerr signal. A maximum in the detected signal ensures that the pump beam is in fact polarized at 45°. At this point we were ready to take the initial Kerr scans. The scan in Figure 4.2 is a set of 250 points collected at 10fs steps of the computer-controlled delay stage.

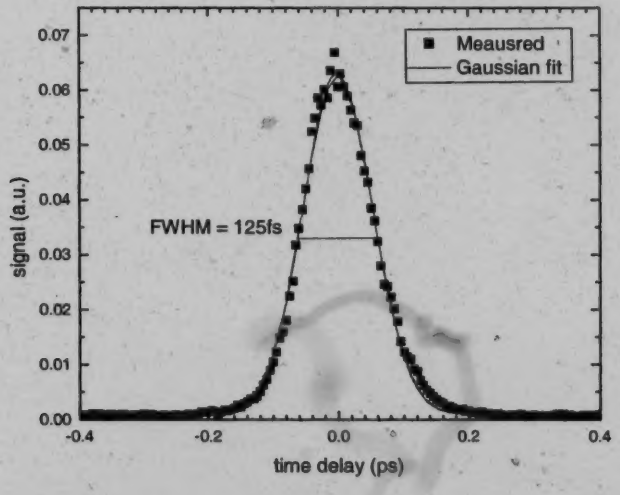

FIGURE 4.2. Kerr signal showing the autocorrelation of the pulse observed in a sample of fused silica. The pulse duration is 125fs at FWHM.

Typically for a Gaussian beam, the pulse width is defined as $1/\sqrt{2} \times$ Full-Width-Half-Maximum (FWHM) of the autocorrelation trace. This produces an estimate for the pulse width $= 1/\sqrt{2} \times 125fs \cong 88fs$. Since we used the fused silica sample as our reference material, we were able to verify this measurement on a daily basis. Any deviations would then indicate possible beam problems.

4.2 *Kerr Gate Characterization*

One of the fundamental aspects of the DOKE setup is that it operates with a linear dependence between the detected signal and pump beam intensity. This contrasts with the homodyne detection technique mentioned in the first chapter, where the detected signal is dependent on the square of the pump intensity. It was necessary to show that the setup indeed exhibits this linear relationship. Figure 4.3 demonstrates the behavior of the detected probe signal modulation, "A-B", on the pump intensity.

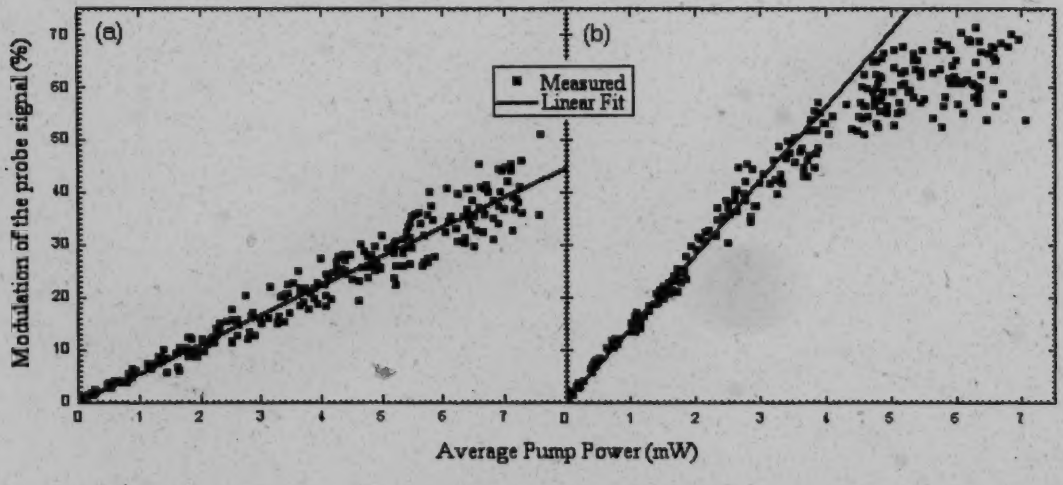

FIGURE 4.3. DOKE signal versus pump intensity. The test was performed using a sample of (a) fused silica and (b) carbon disulfide (CS_2) solution.

Using a sample of fused silica and again using a sample of CS_2 solution, we observed the DOKE Kerr signal while varying the pump beam intensity. As apparent from the plots,

even with "A-B" signal modulation as high as 45%, we have a linear dependence between the Kerr signal and the pump intensity. The data obtained using a sample of fused silica shows great linearity over the entire tested range. It is important, however, to test the limits of the system to get a good idea of the maximum allowable pump beam intensities before the data deviates from the linearity condition mentioned above. The plot for the CS_2 solution shows that above ~45% modulation ($\sin^2\phi' = 0.45$) the linear behavior breaks down. The pump power required to reach such a signal modulation, however, far exceeds the typical powers used in our experiments. Typically, we operated with pump powers which yield no more than 5% signal modulation. These intensities lie well within the linear regime. For most of our samples this corresponds to average powers ranging over about 1 to 3mW.

For the probe signal, large intensities are not required. We chose to use a 50μW probe signal for all measurements. This is more than an order of magnitude smaller than the pump signal but at the same time it is large enough to provide a good signal-to-noise ratio at the photodetectors. Even if the intensity of the probe signal were high enough to induce optical nonlinearities in the sample, small effects of self-phase modulation are undetectable due to the nature of the DOKE setup. Scans were started with probe pulses arriving at the sample just before the pump pulses (negative pump time delay). Under those conditions no Kerr signal is expected ("A-B" signal is 0). Hence this gave us a good reference point and ensured that the obtained signal was induced purely by the intensity of the pump beam. Nevertheless, the probe signal was kept small as to avoid inducing any other possible nonlinear effects such as photodarkening, perhaps or photodamage.

4.3 DOKE Polarization Conditions

As shown in Appendix A, the DOKE setup essentially has four useful pump polarization conditions. One, as discussed earlier, is when the pump beam is polarized at 45° to the analyzer prism and the obtained signal gives us the real part of the nonlinear response, $\sin\phi'/\cos\phi''$. (This was shown earlier in Equation 3.3.) We get the same, but negative, result with pump beam polarized at -45°. Namely this corresponds to an obtained signal of $-\sin\phi'/\cos\phi''$. Similarly, the signal corresponding to the imaginary component of the nonlinear response is obtained by setting the pump beam polarization to 0° or 90° to the axis of the analyzer prism. To show that this prediction is indeed consistent with the results of our DOKE setup, we used a sample of CS_2 to perform four separate scans. One for each of the four polarization conditions. The results are shown in Figure 4.4.

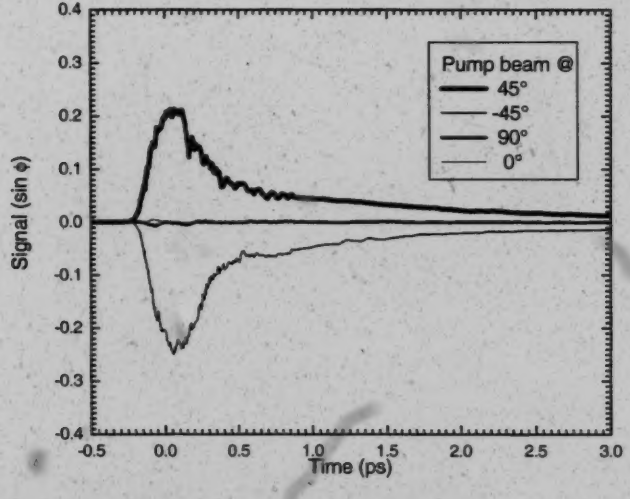

FIGURE 4.4. DOKE signal for a sample of CS_2 obtained at the four different pump beam polarization conditions at λ=1390nm.

As expected, we observe a mirroring in the detected signals of CS_2 at pump polarizations of +45° and -45°. The other two signals are zero. This is also expected since CS_2 does not have any two-photon absorption at the wavelengths used in our experiment [27]. This clearly shows that the setup complies with the predictions and adds further evidence that we have a properly working Kerr gate. Slight variations in the shapes of the obtained traces can be attributed to noise and non-ideal alignment of the pump beam half-wave plate.

4.4 Measurements on Carbon Di-sulfide (CS_2)

CS_2 is a liquid that is commonly used as a reference material for optical Kerr spectroscopy. Primarily, it possesses large Kerr nonlinearities and low two-photon absorption. The Kerr response of the CS_2 solution is attributed to two separate Kerr mechanisms. Those are a smaller instantaneous electronic Kerr response, and a dominant molecular reorientation response. Figure 4.5 shows the time resolved Kerr response of CS_2 measured at a wavelength of 1390 nm. It clearly displays a two-peak response with the first peak centered around zero pump delay time, which is representative of the instantaneous electronic Kerr response. The second peak is shifted to the positive pump delay time indicating a non-instantaneous response attributed to the molecular reorientation. The long exponential

decay tail corresponds to the molecular relaxation of the CS_2 solution. The relaxation time of $\tau = 1.59ps$ is in close agreement with $\tau = 1.61ps$ reported for CS_2 in the literature [68].

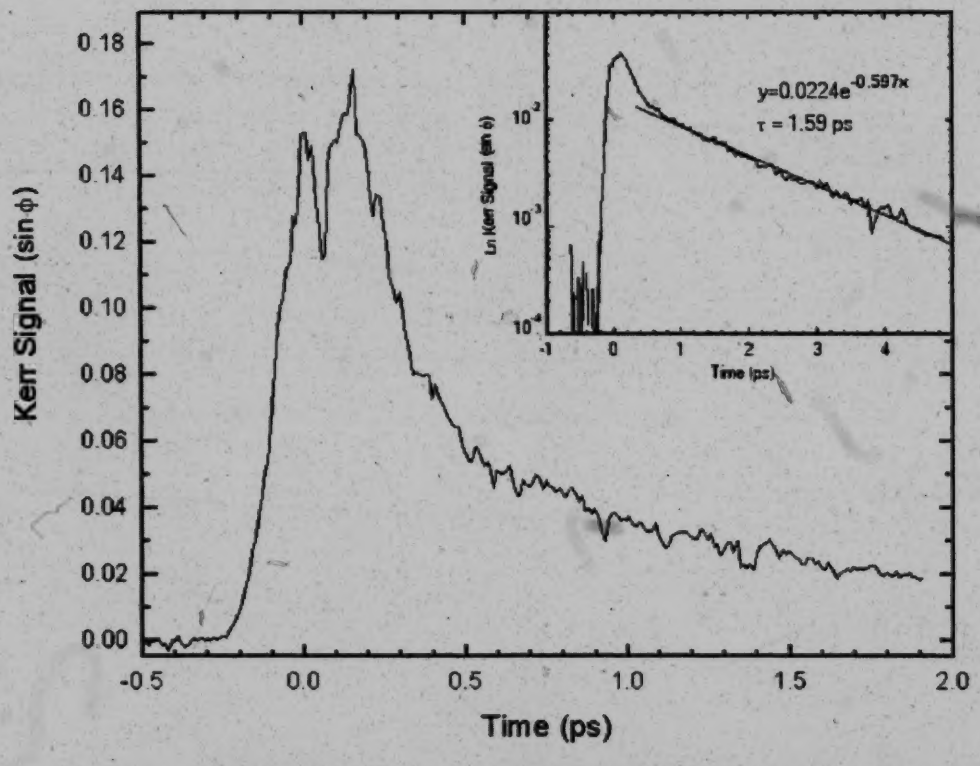

FIGURE 4.5. Time-resolved Kerr scan of CS_2 at λ=1390nm, showing a double-peak and an exponential decay response indicating electronic and molecular orientational contributions to the Kerr signal. Inset trace is a log plot of the result showing the relaxation time, τ=1.59 ps, in the decay tail.

4.5 *Measurements on Fused Silica (SiO_2)*

Fused silica is another reference material very commonly used in optical Kerr spectroscopy. Its well characterized Kerr response, documented in the literature, makes it a good starting point for verifying the proper operation of the system. Its purely electronic Kerr response also makes it useful for performing daily measurements of the pulse duration as mentioned in the section §4.1.2. Figure 4.6 shows a time resolved Kerr scan of the fused silica sample.

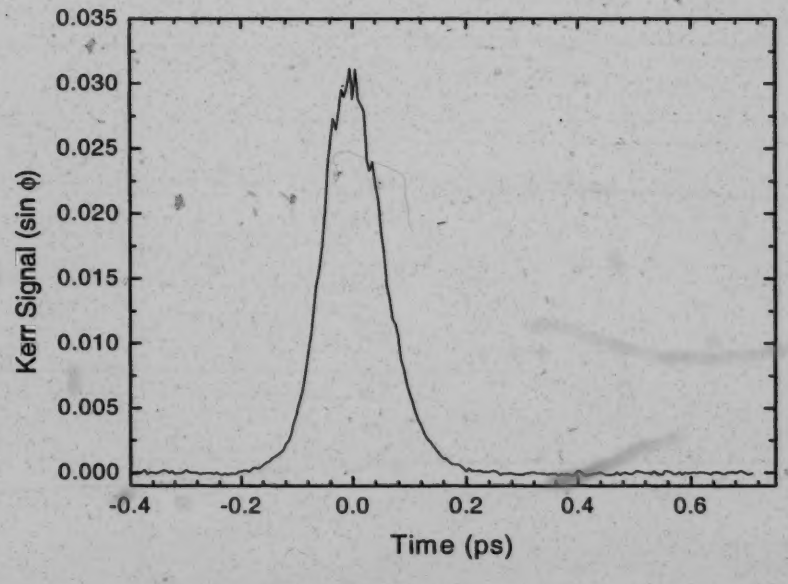

FIGURE 4.6. Time-resolved Kerr scan of SiO_2 at λ=1425nm. From the symmetric Gaussian shape, which represents the autocorrelation of the laser pulse, it is evident that the Kerr response is purely electronic.

Performing numerous such scans over the course of the DOKE system testing phase, we observed average SiO_2 Kerr coefficient value of

$$n_2 = 2.68 \pm 0.45 \times 10^{-20}\ m^2/W. \qquad \text{(Eq. 4.2)}$$

This number compares favorably with the widely reported SiO_2 Kerr coefficient value [15][50][69-72] in the same wavelength region. Although the system is capable of performing absolute measurements, we calculate and report the Kerr coefficients of As_2Se_3 samples as relative to the n_2 of fused silica. Sample calculations are provided in the Appendices. We performed Kerr scans of all our samples in close succession with the Kerr scans of the fused silica sample, allowing for individual referencing of each sample signal. Reporting relative values in this manner has the advantage of reduced uncertainty in the results. Otherwise errors can be caused by day-to-day variations of laser beam quality and alignment. The nonlinearity values for any sample is obtained directly from the DOKE peak signals using

$$n_{2S} = n_{2R}\left(\frac{\phi_S d_R}{\phi_R d_S}\right), \qquad \text{(Eq. 4.3)}$$

where n_{2S} is the Kerr coefficient of the sample, and n_{2R} is the Kerr coefficient of the reference material, which in our case is fused silica and is given by the Equation 4.2. The values ϕ_S and ϕ_R are, respectively, the measured polarization rotation of the sample and the reference material, and d_S and d_R are the respective thicknesses of the sample and the reference. The derivation of Equation 4.3 is given in Appendix C.

Having demonstrated a properly functioning Kerr gate, we proceeded with studying Kerr dynamics in As_2Se_3 chalcogenide glass samples.

4.6 Measurement Details

The laser light produced by the Optical Parametric Amplifier (OPA) exhibits relatively poor stability. We needed to perform numerous runs on all our samples (including fused silica) in order to ensure good repeatability and reportable results. Each run involved performing three Kerr scans; one for the fused silica sample to provide a reference signal, one for the film on substrate sample, and one for only the substrate. The Kerr coefficient for the sample is then calculated using

$$n_{2F} = n_{2R}\left[\frac{\phi_S}{\phi_B} - 1\right]\left[\frac{\phi_B d_R I_R}{\phi_R d_F I_F}\right]. \qquad \text{(Eq. 4.4)}$$

Here, n_{2R} is the Kerr coefficient of our chalcogenide glass film sample, ϕ_B is the measured polarization rotation of the film substrate alone, and d_F is the thickness of the deposited film. The pump beam intensities used during Kerr scan of the film sample, I_F, and of the reference sample, I_R, would normally be equal, I_R=I_F, and would cancel out of the equation. However, to account for the possibility of OPA laser power drifts between subsequent scans, the two terms are included in the equation for improved accuracy. The derivation of Equation 4.4 is provided in Appendix D.

Before starting measurements each day, we realigned the pump and probe signals at the sample, in space and time, and set the average powers to 50μW for the probe and 1-3mW

for the pump. With the fused silica sample in the sample holder, we fine-adjusted our optics to yield maximum Kerr signal. We then recorded the average powers of the beams and the readings of all photodetectors from the lock-in amplifiers for future reference. This gave a good starting point each day and would indicate potential problems when readings differed by an appreciable amount. Since long-term stability in the overlap of the pump and probe beams is difficult to attain, we typically repeated this process several times a day during the experimental stage, as alignment drifts became apparent. Performing a reference scan of fused silica for each run also provided a good indication of possible problems during data collection or at least during data analysis.

Our three photodetectors, the "A-B", "A+B" and the pre-sample pump/probe reference photodetectors, were connected to separate lock-in amplifiers, in turn connected to a computer for data collection. The "A+B" and the reference photodetector signals were detected by the lock-in amplifiers at the laser repetition frequency of 1.08KHz, while the "A-B" photodetector signal was detected at the chopper frequency of 270Hz (1.08KHz/4 synchronized with the laser output). We set the integration constant on the lock-in amplifiers to 100ms. At the computer, the data was averaged and collected every 300ms. In hope of further improving the detected signal to noise ratio, we increased the integration constants as high as 300ms for the lock-in amplifiers and 900ms for the computer but this did not produce appreciably improved results. We stayed with our original settings of 100ms and 300ms for the lock-in amplifiers and the computer, respectively, hence keeping the duration of the Kerr scans relatively short.

4.7 Measurements on As_2Se_3 Films

4.7.1 Sample Preparation

Two samples of amorphous chalcogenide (As_2Se_3) thin films were deposited by thermal evaporation of the melt quenched glassy material onto BK-7 glass substrate. All films were deposited onto an unheated (room temperature) substrate. The thermal evaporation process was performed inside a coating system at a base pressure of $2\times10^{-6}Torr$. During the deposition process, the substrate was rotated by means of a planetary rotation system in order to obtain homogeneous films of uniform thickness. The deposition rate was typically $\approx 20nm/s$. The resulting thickness of the two As_2Se_3 films, which was measured using contact profilometry, was 4.5μm and 16μm.

The film composition of the evaporated films was measured by an electron microprobe analyzer (EDAX) on different spots (spot size $\approx 2nm$). The composition of the films was found to be uniform within the measurement accuracy of about 0.5%. The chemical composition of the deposited films was very close that of the starting bulk material. The linear transmission and dispersion measurements of As_2Se_3 glass, performed by a University of Alberta group[73], are shown on Figure 4.7. With a band edge around $\lambda \approx 690nm$, As_2Se_3 has a bandgap of about 1.79eV.

Before deposition, part of each substrate was covered by a piece of teflon tape. As a result, a piece of the substrate is left exposed after the deposition process. Performing a Kerr scan on the bare part of the substrate enabled us to later separate the substrate's contribution to the detected Kerr signal from the subsequent substrate + film scan.

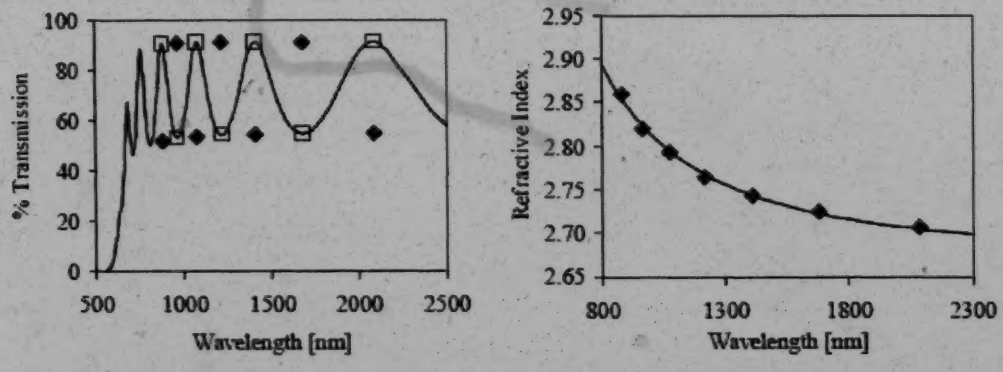

FIGURE 4.7. Transmission spectrum and dispersion relation of As_2Se_3[73].

4.7.2 Time-Resolved Scans

Figure 4.8 shows representative time-resolved Kerr signals of the As_2Se_3 samples, including the contribution of the BK-7 glass substrate. The corresponding signals obtained from the substrates alone are included in the figure insert. As described in Chapter 3, $sin\phi'$ is obtained by dividing the "A-B" by the "A+B" and the normalized reference photodetector signals. The only modifications made to the raw Kerr signals was a slight shifting of the signal levels to yield a zero baseline at negative pump delay times. The data shown is not normalized to the fused silica reference. This normalization was done during the n_2 calculations.

The Kerr signal obtained from the BK-7 glass is small (comparable to that obtained for fused silica) and purely of electronic origin. Consequently, the time resolved profile

obtained for the film and substrate together accurately represents the signal that would be obtained for As_2Se_3 alone, except for its magnitude. In many of our scans we noticed a presence of sometimes excessive on-peak noise. This effect has been noticed by many research groups and has been attributed to transient coherent effects [68][74]. These effects can be minimized with the right adjustment of the pick-off mirror M_p [27]. However, this is nearly impossible to do with a laser beam exhibiting spatial jitter such as the OPA beam used in our setup. This on-peak noise greatly contributes to the uncertainties in our n_2 values, since only the peak values in the time-resolved scans contribute to the calculation of the nonlinear coefficients. We minimized these uncertainties by averaging our results. Each of the samples was scanned numerous times, in order to increase our confidence in the numbers reported.

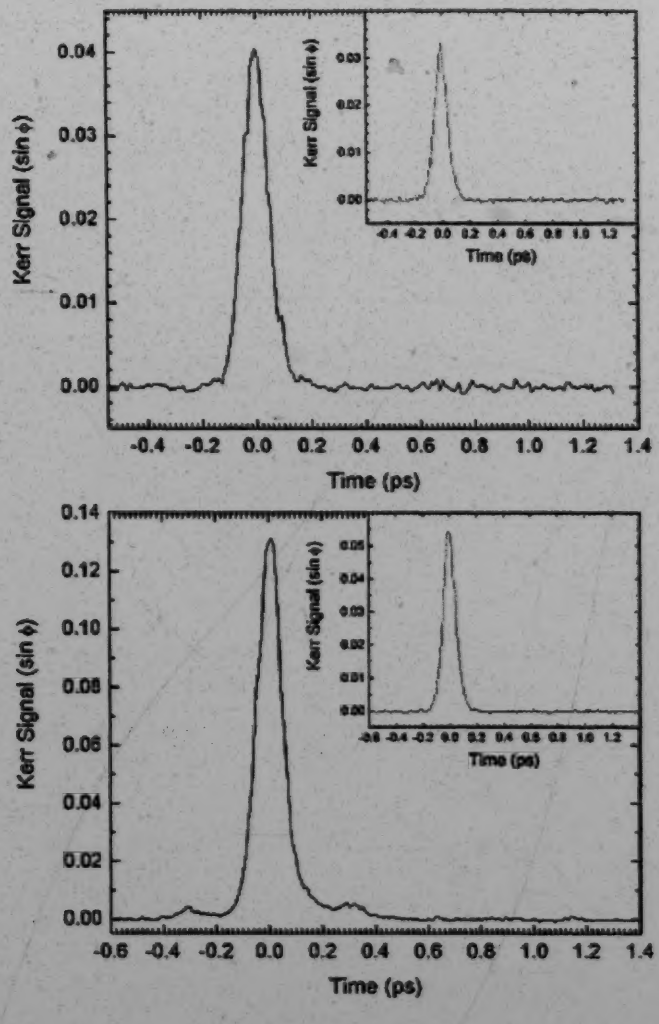

FIGURE 4.8. DOKE Kerr scan of As_2Se_3, 4.5μm thick (top) and 16μm thick (bottom) films deposited on BK-7 glass, at a wavelength λ=1425nm. DOKE scan of the corresponding BK-7 substrate alone is included in the inset.

Observing the temporal dynamics of the Kerr response we note that it appears to be purely of electronic origin. The symmetric Gaussian shape indicates an instantaneous response that follows the autocorrelation of the pulse.

In all scans of the 16μm thick film, two humps appear on each side of the pulse. The first peak cannot be a real response as it shows up at negative pump delay time, $\tau \approx -300fs$. Further analysis revealed that this is attributed to the reflections of the probe beam in the film sample due to large index mismatch between the film and the substrate or air. The index of refraction of As_2Se_3 at the wavelength used in the experiment is around 2.75, which yields glass-substrate interface reflectance $R_s = 0.09$, and glass-air interface reflectance $R_a = 0.22$. This means that about 2% of the probe light makes a double pass through the sample. Taking the speed of light and multiplying by the time delay, $\tau = 300fs$, we get $2dn = 90\mu m$. With $n = 2.75$ for As_2Se_3 glass, we get $d \cong 16\mu m$ which is the thickness of our film sample. Consequently, at pump delay time $\tau \approx -300fs$, the reflected probe pulse meets the delayed pump pulse and they travel together through the sample in the same manner as the nonreflected probe and pump pulses at zero delay time. This gives rise to the observed secondary peak, which has a magnitude that is about 2% of the main peak at zero pump delay. The same thing can be said for the second hump, which peaks at $\tau \approx 300fs$. Here, however, it is the reflection of the pump beam inside the sample which meets with the delayed probe pulse and hence gives rise to the second false peak at $\tau = 300fs$.

From the Kerr scan obtained above we are potentially able to extract the nonlinear absorption coefficient by simply comparing the data collected by the pre-sample reference detec-

tor and the post sample "A+B" detector. However, due to a noisy laser source, no nonlinear absorption was observed in this manner. Consequently, we moved to the second polarization condition of the pump beam ($\theta = 0°$), and proceeded to measure the sample nonlinear absorption directly. For this measurement we used the 16μm As_2Se_3 sample. Figure 4.9 shows the average of two subsequent nonlinear absorption scans.

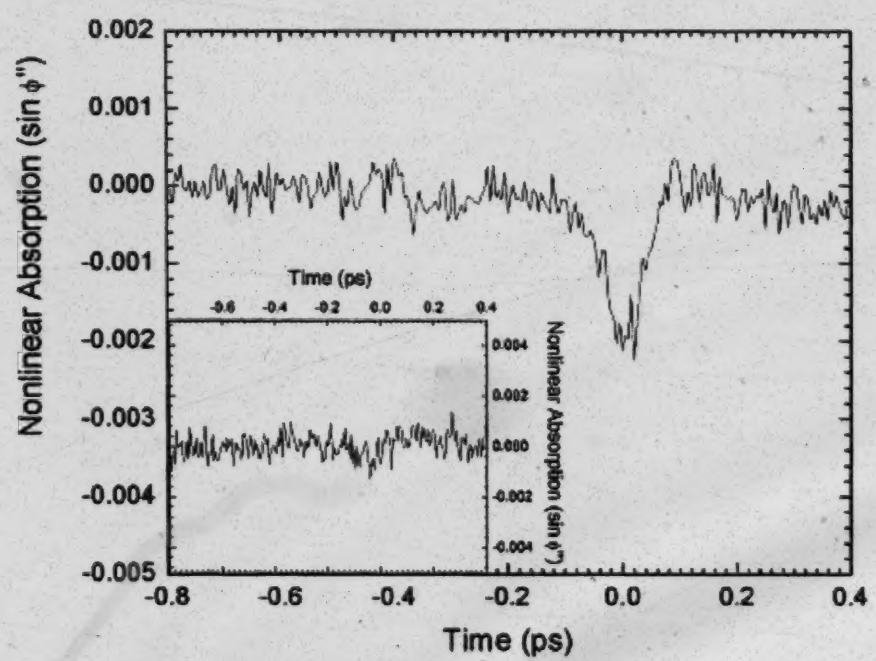

FIGURE 4.9. DOKE nonlinear absorption scan (pump polarization θ=0°) of the 16μm, As_2Se_3 film deposited on BK-7 glass, at a wavelength λ=1425nm. The fused silica zero reference scan is included in the inset.

To ensure good repeatability we performed numerous scans on each sample. Using peak, nonlinear phase shift values recorded for each scan with Equation 3.1, we arrived at the sought after Kerr coefficient, n_2. Similarly, using Equation 3.2 and the second DOKE condition results, we calculated the two-photon absorption coefficient, β, for our thicker sample. Since the two-photon absorption signal from the 16μm sample was already quite small, we did not attempt to perform this measurement on the thinner, 4.5μm sample. Table 4.1 summarizes our results.

Sample	Kerr coefficient n_2 (m^2/W)	Absorption coefficient β (m/W)
SiO_2	$2.68 \pm 0.45 \times 10^{-20}$	N/M
As_2Se_3 – 4.5μm	$6.90 \pm 2.2 \times 10^{-18}$	N/M
As_2Se_3 – 16μm	$6.71 \pm 0.7 \times 10^{-18}$	0.14×10^{-11}

*N/M – Not measured.

TABLE 4.1. DOKE experimental results.

The large uncertainty in the Kerr coefficient of the 4.5μm film is attributed to the surface nonuniformity of the film. The induced Kerr signal in the thinner sample is quite small compared to the Kerr signal of the 1.5mm substrate. Although the nonlinear Kerr coefficient of the BK-7 glass is quite small (comparable to the n_2 of fused silica), the interaction length is much larger compared to the 4.5μm interaction length in the film. In other words, it is harder to isolate the thinner film's contribution to the nonlinear phase shift as it is

mostly swamped by the signal from its substrate, resulting in the increased uncertainty in the measurement. In addition, although we did not examine the film surface in detail, many pinholes in the sample were clearly visible when placed against a source of light. Typically, we tried to stay clear from the damaged spots on the sample. However, other less obvious surface irregularities might have been present, contributing to the noise in the detected Kerr signal. Nevertheless, even though the results for the 16μm sample were much more repeatable from scan to scan, the two samples yielded virtually the same Kerr coefficient. The samples also show good agreement with the values reported in the literature for bulk As_2Se_3 samples, obtained at similar wavelength and measurement laser intensity. Table 4.2 shows a summary of our results together with the ones found in the literature.

$n_2 \times 10^{-18}$ (m^2/W)	$\beta_2 \times 10^{-11}$ (m/W)	Measurement Intensity (GW/cm^2)	Measurement Wavelength (nm)	Measurement Technique	Source
6.2	<0.3	9.5	1400	Z-scan	[61]
6.5	N/R	20	1600	Z-scan	[66]
6.7	0.14	11	1425	DOKE	This work
10	0.01	0.16-4.4	1430	Z-scan	[51]
11	0.4	2-4	1500	Z-scan	[11]
23	0.14	0.2	1550	SRTBC	[62]

*N/R – not reported.

TABLE 4.2. Reported Kerr and two photon absorption coefficients for the As_2Se_3 in the 1400-1600nm wavelength range.

CHAPTER 5

Conclusions and Future Work

An optical Kerr gate employing a detection technique known as differential optical Kerr effect (DOKE) has been designed, built and tested. As a light source, the DOKE setup utilizes a wavelength tunable, optical parametric amplifier (OPA) pumped by a 800nm, 100fs laser pulses at a repetition rate of 1kHz. The setup is capable of performing Kerr scans anywhere in the 1250nm to 1600nm wavelength range. DOKE detection represents a considerable improvement to the optical heterodyne Kerr detection technique. The signal detection is both simpler and more intuitive than the heterodyne technique, while maintaining the ability to separate the real and imaginary components of the third-order nonlinear susceptibility. Furthermore, the DOKE technique provides Kerr response signals that are linear in both pump and probe beam intensities and offer a larger dynamic range of linear

signal behavior compared with other techniques. Both mathematical and physical descriptions of DOKE detection have been given, with the goal of presenting proof of proper detection as well as instruction to those who may wish to use DOKE detection as their Kerr gate technique.

DOKE detection technique was used to study Kerr dynamics of As_2Se_3 thin film glass samples. We have found the Kerr coefficient to be in good agreement with the Kerr coefficient of bulk As_2Se_3 samples documented in literature for similar wavelengths. The glass exhibits an ultra-fast response time that follows the autocorrelation of the pulse, and shows no evidence of slow decay components when probed with 100fs laser pulses. We have also found the two-photon absorption coefficient $\beta = 0.14\times10^{-11} m/W$, which, together with the obtained n_2 value, yields a figure of merit $FOM \approx 3.5$. As a material, which in general presents the highest third-order nonlinear properties among the different families of glasses, chalcogenide glass is already becoming the material of choice in applications of integrated, all-optical signal processing devices and nonlinear waveguide fabrication.

A large nonlinear response in a short interaction length, as offered in integrated structures, requires a large reduction in the mode field area, accompanied by a large Kerr nonlinearity of the waveguide material. Such waveguide structures are possible with the use of highly nonlinear chalcogenide glasses and numerous researchers are already investigating various methods for fabrication of small core, high-index-contrast chalcogenide waveguide structures [75][76].

One research group reports the fabrication of As_2S_3 rib waveguides, with small effective mode area $A_{eff} = 4.2\mu m^2$ [75]. They observe large nonlinear phase shifts in only 6cm long

waveguides. Even larger phase shifts can be achieved with use of the more nonlinear As_2Se_3 instead of As_2S_3 [17]. All-optical regeneration based on self-phase modulation (SPM) in single mode, 6μm core diameter, As_2Se_3 chalcogenide fiber has already been demonstrated [16]. This fully passive device, which included only 2.8m of chalcogenide fiber, operated with 5.8ps duration pulses suitable for 40Gb/s systems, and with peak powers <10W. With peak power of ~8W, the device provides an SPM-induced phase-shift that is sufficient for operation, and is close to practical device power levels.

As a result of recent advancements in low-loss rib waveguides and high quality bragg gratings in chalcogenide glass, a terabit per second, fully integrated, As_2S_3 based, all-optical signal regenerator has already been fabricated [17]. It operates with 1.4ps pulses at peak power levels from a few up to few 10s of watts. This was achieved in a 5cm long waveguide, 4μm wide and 1.1μm high, which already makes for a significantly compact device.

Considerable attention has also been given to silver doped chalcogenide glasses. The addition of Ag into an As_2Se_3 guiding layer increases its index of refraction and its optical nonlinearity, $\chi^{(3)}$ [76]. The increase in index of refraction allows for fabrication of better confining structures and waveguides, while the increase in nonlinearity allows for more efficient optical signal processing devices. Large amounts of Ag can be dissolved in amorphous chalcogenide layers (in general up to 30-40 wt%) yielding large increase in $\chi^{(3)}$ nonlinearities [77]. One thing to note, however, is that there is an optimal limit of silver concentration in a given chalcogenide film. With increasing concentration of silver, the

optical transmittance of the glass decreases, which in turn decreases the materials' figure of merit and its usability for all-optical signal processing [31][77].

A few interesting and fundamental issues regarding nonlinear behavior in chalcogenide glasses, however, have still not been fully resolved. Higher order nonlinearities in these glasses have not yet been fully characterized. Three-, four-, and five-photon absorption processes have been reported [64][78], and an intensity dependent (effective) n_2 has been attributed to self-defocusing 5^{th} order nonlinearity [31][79]. Second, the spectral dependence of the nonlinear response has not been studied in detail.

Most of these still outstanding questions can be answered with the aid of the DOKE setup demonstrated here for measuring time-resolved, third-order nonlinearities of thin films. With the OPA as the system's light source, we have the versatility of easily measuring the nonlinear behavior of films at any wavelength between 1250nm and 1600nm. The easily adjustable pump beam intensity gives us the versatility of probing films for presence of intensity dependent mechanisms and higher order nonlinearities. Due to presented difficulties with our laser source, these results will be presented in our future works.

In summary, we can clearly see that as researchers keep reporting on better and better device design and waveguide fabrication techniques, we come closer to achieving ultra-fast, all-optical signal processing networks. Chalcogenide glasses, such as As_2S_3 and As_2Se_3, will allow us to achieve this on an integrated scale.

REFERENCES

[1] H. M. Gibbs, G. Khitrova, N. Peyghambarian. 1990. *Nonlinear Photonics.* Springer-Verlag Berlin Heidelberg. Berlin.

[2] Bahaa E.A. Saleh, M.C. Teich. 1991. *Fundamentals of Photonics.* John Wiley & Sons, Inc., New York.

[3] *A brief history of optics.* Retrieved January 2005. http://www.cartage.org.lb/en/themes/Sciences/Physics/Optics/briefhistory/briefhistory.htm

[4] 1983 IEEE Annual Awards Presentation Brochure. *IEEE history centre - Legacies.* http://www.ieee.org/organizations/history_center/legacies/bloembergen.html

[5] Based on the book: *Laser pioneer interviews.* Retrieved January 2005. http://www.lasing.com/paginas/archivos/his_first.htm

[6] L. Garwin, T. Lincoln, editors. 2003. *A Century of Nature: Twenty-One Discoveries that Changed Science and the World.* http://www.press.uchicago.edu/Misc/Chicago/284158_townes.html

[7] T. H. Maiman. 1960. *Stimulated optical radiation in ruby,* Nature 187:493-494.

[8] Retrieved January 2005. *John Kerr.* http://www.technologyscotland.org/pioneering/light_years_black.html

[9] M. W. Davidson, Florida State University. 1995. *Pioneers in optics - John Kerr (1824-1907).* http://micro.magnet.fsu.edu/optics/timeline/people/kerr.html

[10] Wikipedia - The Free Encyclopedia. Retrieved January 2005. *John Kerr (physicist).* http://en.wikipedia.org/wiki/John_Kerr_(physicist)

[11] G. Lenz, J. Zimmermann, T. Katsufuji, M. E. Lines, H. Y. Hwang, S. Spalter, R. E. Slusher, S.-W. Cheong. 2000. *Large Kerr effect in bulk Se-based chalcogenide glasses.* Optics Letters. 25(4):254-256.

[12] M. J. Potasek, Y. Yang. 2002. *Multiterabit-per-second All-Optical Switching in a Nonlinear Directional Coupler.* IEEE Journal of Selected Topics in Quantum Electronics. 8(3):714-720.

[13] P. N. Prasad, D.J. Williams. 1991. *Introduction to nonlinear optical effects in molecules and polymers.* John Wiley & Sons, Inc. Toronto.

[14] A. Andriesh, V. Chumash. 1998. *Nonlinear optical phenomena in chalcogenide glasses.* Pure and Applied Optics. 7:351-360.

[15] S. Spälter, G. Lenz, R.E. Slusher, H.Y. Hwang, J. Zimmermann, T. Katsufuji, S-W. Cheong, M.E. Lines. 2000. *Highly Nonlinear Chalcogenide Glasses for Ultrafast All-Optical Switching in Optical TDM Communication Systems.* Conference-on-Optical-Fiber-Communication. 3:137-139.

[16] L. B. Fu, M. Rochette, B. G. Ta'eed, D. J.Moss, B. J. Eggleton. 2005. *Investigation of self-phase modulation based optical regeneration in single mode As_2Se_3 chalcogenide glass fiber.* Optics Express. 13(19):7637-7644.

[17] V. G. Ta'eed, M. Shokooh-Saremi, L. Fu, D. J. Moss, M. Rochette, I. C. M. Littler, B. J. Eggleton. 2005. *Integrated all-optical pulse regenerator in chalcogenide waveguides.* Optics Letters. 30(21):2900-2902.

[18] H.-M. Keller, S. Pereira, J.E. Sipe. 1999. *Grating Enhanced All-Optical Switching in a Mach-Zender Interferometer.* Optics Communications. 170:35-40.

[19] S. Pereira, P. Chak, J. E. Sipe. 2003. *All-optical AND gate by use of a Kerr nonlinear microresonator structure.* Optics Letters. 28(6):444-446.

[20] John Mauro. 2003. *Nonlinear Optical Switching with Sagnac Interferometers.* www.homepage.mac.com/maurojc/papers/pdf/sagnac.pdf.

[21] I. S. Fogel, J. M. Bendickson, M. D. Tocci, M. J. Bloemer, M. Scolora, C. M. Bowden, J. P. Dowling. 1998. *Spontaneous Emission and Nonlinear Effects in Photonic Bandgap Materials.* Pure and Applied Optics. 7:393-407.

[22] R. E. Slusher, B. J. Eggleton. 2003. *Nonlinear Photonic Crystals.* Springer-Verlag Berlin, Heidelberg.

[23] G. Boudebs, G. Sanchez, J. Troles, F. Smektala. 2001. *Nonlinear optical properties of chalcogenide glass: comparison between Mach-Zender interferometry and Z-scan techniques.* Optics Communications. 199:425-433.

[24] I. Kang, T. Krauss, F. Wise. 1997. *Sensitive measurement of nonlinear refraction and two-photon absorption by spectrally resolved two-beam coupling.* Optics Letters. 22(14):1077-1079.

[25] P. W. Smith, W. J. Tomlinson, D. J. Eilenberger, P. J. Maloney. 1981. *Measurement of electronic optical Kerr coefficients.* Optics Letters. 6(12):581-583.

[26] M. E. Orczyk, M. Samoc, J. Swiatkiewicz, N. Manickam, M. Tomoaia-Cotisel, P. N. Prasad. 1992. *Optical heterodyning of the phase-tuned femtosecond optical Kerr gate signal for the determination of complex third-order susceptibilities.* Applied Physics Letters. 60(23):2837-2839.

[27] A. D. Slepkov. 2002. *Third-order nonlinearities in novel iso-polydiacetylenes studied by a differential optical Kerr detection technique.* Thesis (M.Sc.) - University of Alberta.

[28] M. Sheik-Bahae, A. A. Said, T. Wei, D. J. Hagan, E. W. Van Stryland. 1990. *Sensitive Measurement of Optical Nonlinearities Using a Single Beam.* IEEE Journal of Quantum Electronics. 26(4):760-769.

[29] M. Sheik-bahae, A. A. Said, E. W. Van Stryland. 1989. *High-sensitivity, Single-beam n_2 Measurements.* Optics Letters. 14(17):955-957.

[30] Y. M. Cheung, S. K. Gayen. 1994. *Optical Nonlinearities of Tea Studied by Z-scan and Four-wave Mixing Techniques.* Journal of Optical Society of America B. 11(4):636-643.

[31] K. Ogusu, J. Yamasaki, S. Maeda. 2004. *Linear and Nonlinear Optical Properties of Ag-As-Se Chalcogenide Glasses for All-optical Switching.* Optics Letters. 29(3):265-267.

[32] J. M. Harbold, F. W. Wise, B. G. Aitken. 2001. *Se-based chalcogenide glasses 1000 times more nonlinear than fused silica.* Conference on Lasers and Electro-Optics (CLEO) Europe - Technical Digest. 14-15.

[33] S. Smolorz, F. Weise, N. F. Borrelli. 1999. *Measurement of the nonlinear optical response of optical fiber materials by use of spectrally resolved two-beam coupling.* Optics Letters. 24(16):1103-1105.

[34] E. G. Sauter. 1996. *Nonlinear Optics.* John Wiley & Sons, Inc., New York.

[35] J. H. Hoffman. 1986. *Thermally Induced Degenerate Four-Wave Mixing.* IEEE Journal of Quantum Electronics. 22(4):552-562.

[36] A. D. Slepkov, F. A. Hegmann, Y. Zhao, R. R. Tykwinski, K. Kamada. 2002. *Ultrafast Optical Kerr Effect Measurements of Third-Order Nonlinearities in Cross-Conjugated iso-Polydiacetylene Oligomers.* Journal of Chemical Physics. 116(9):3834-3840.

[37] J. E. Aber, M. C. Newstein, B. A. Garetz. 2000. *Femtosecond Optical Kerr Measurements in Silicate Glasses.* Journal of Optical Society of America B. 17(1)120:127.

[38] X. F. Wang, Z. W. Wang, J. G. Yu, C. L. Liu, X. J. Zhao, Q. H. Gong. 2004. *Large and Ultrafast Third-Order Optical Nonlinearity of GeS_2 - Ga_2S_3 -CdS Chalcogenide Glass.* Chemical Physics Letters. 399:230-233.

[39] S. Montant, A. Le Calvez, E. Freysz, A. Cucasse, M. Couzi. 1998. *Time-Domain Separation of Nuclear and Electronic Contributions to the Third-Order Nonlinearity in Glasses.* Journal of Optical Society of America B. 15(11):2802-2807.

[40] R. Fedosejevs. 2003. *Nonlinear Optics.* EE 684 class notes - University of Alberta. Chapter 1.

[41] A. E. Siegman. 1986. *Lasers.* University Science Books. Mill Valley, California.

[42] R.W. Boyd. 2003. *Nonlinear Optics.* Academic Press, San Diego, California.

[43] Amnon Yariv. 1989. *Quantum Electronics.* John Wiley & Sons, Inc., New York. p482-484.

[44] A. Feldman, D. Horwitz, R. M. Waxler. 1973. *Mechanisms for Self-Focusing in Optical Glasses.* IEEE Journal of Quantum Electronics. 9(11):1054-1061.

[45] L. Brzozowski, E. H. Sargent. 2001. *Azobenzoates for Photonic Network Applications: Third-Order Nonlinear Optical Properties.* Journal of Materials Science: Materials in Electronics. 12:483-489.

[46] S. Smolorz, I. Kang, F. Wise, B. G. Aitken, N. F. Borelli. 1999. *Studies of Optical Non-linearities of Chalcogenide and Heavy-metal Oxide Glasses.* Journal of Non-Crystalline Solids. 256&257:310-317.

[47] S. L. Danielson, C. Joergensen, M. Vaa, B. Mikkelsen, K. E. Stubkjaer, P. Doussiere, F. Pommerau, L. Goldstein, M. Gois. 1996. *Bit error rate assessment of a 40 Gb/s all-optical polarization independent wavelength converter.* Electronics Letters. 32:1688-1690

[48] J. T. Gopinath, M. Soljacic, E. P. Ippen, V. N. Fuflyigin, W. A. King, M. Shurgalin. 2004. *Third Order Nonlinearities in Ge-As-Se Based Glasses for Telecommunications Applications.* Journal of Applied Physics. 96(11):6931-6933.

[49] J. M. Harbold, F. O. Ilday, F. W. Wise, B. G. Aitken. 2002. *Highly Nonlinear Ge-As-Se and Ge-As-S-Se Glasses for All-Optical Switching.* IEEE Photonics Technology Letters. 14(6):822-824.

[50] F. Smektala, C. Quemard, V. Coudrec, A. Barthelemy. 2000. *Non-linear Optical Properties of Chalcogenide Glasses Measured by Z-Scan.* Journal of Non-Crystalline Solids. 274:232-237.

[51] C. Quemard, F. Smektala, V. Coudrec, A. Barthelemy, J. Lucas. 2001. *Chalcogenide Glasses with High Non Linear Optical Properties for Telecommunications.* Journal of Physics and Chemistry of Solids. 62(8):1435-1440.

[52] M.E. Lines. 1991. *Oxide Glasses for Fast Photonic Switching: A Comparative Study.* Journal of Applied Physics. 69:6876-6884.

[53] J.M. Gonzalez-Leal, M. Vlcek, R. Prieto-Alcon, A. Stronski, T. Wagner, E. Marquez. 2003. *Thermal relaxation of the structural and optical properties of amorphous $As_{40}S_{60-x}Se_x$ films.* Journal of Non-Crystalline Solids. 326&327:146-153.

[54] K. Petkov, P.J.S. Ewen. 1999. *Photoinduced changes in the linear and non-linear optical properties of chalcogenide glasses.* Journal of Non-Crystalline Solids. 249:150-159.

[55] N.L. Boling, A.J. Glass, A. Owyoung. 1978. *Empirical relationships for predicting nonlinear refractive index changes in optical solids.* IEEE Journal of Quantum Electronics. QE-14: 601-608.

[56] C. Aversa, J.E. Sipe, M. Sheik-Bahae, E.W. Van Stryland. 1994. *Third-order optical nonlinearities in semiconductors: the two-band model.* Physical Review B 50:18073-18082.

[57] R. DeSalvo, A.A. Said, D.J. Hagan, E.W. Van Stryland, M. Sheik-Bahae. 1996. *Infrared to ultraviolet measurements of two-photon absorption and n2 in wide bandgap solids.* IEEE Journal of Quantum Electronics. 32:1324-1333.

[58] Y-F Chen, K. Beckwitt, T.W. Wise, B.G. Aitken, J.S. Sanghera, I.D. Aggrawal. 2006. *Measurement of fifth- and seventh-order nonlinearities of glasses.* Journal of Optical Society of America B. 23(2):347:352.

[59] M. Frumar, J. Jedelsky, B. Frumarova, T. Wagner, M. Hrdlicka. 2003. *Optically and thermally induced changes of structure, linear, and non-linear optical properties of chalcogenide thin films.* Journal of Non-Crystalline Solids. 326&327:399-404.

[60] N.F. Mott, E.A. Davis. 1979. *Electronic Processes in Non-Crystalline Materials.* Clarendon, Oxford.

[61] A. Tomalik, R. G. Decorby, A. D. Slepkov, F. A. Hegmann, A. Major, P.W.E. Smith, J. S. Aitchison. 2005. *Ultrafast time-resolved and spectrally resolved measurement of third-order nonlinearities in As_2Se_3 chalcogenide glass.* Proceedings of SPIE. 5971.

[62] J. M. Harbold, F. O. Ilday, F. W. Wise, J. S. Sanghera, V. Q. Nguyen, L. B. Shaw, I. D. Aggarwal. 2002. *Highly Nonlinear As-S-Se Glasses for All-Optical Switching.* Optics Letters. 27(2):119-121.

[63] F. Smektala, C. Quemard, L. Leneindre, J. Lucas, A. Barthelemy, C De Angelis. 1998. *Chalcogenide Glasses with Large Non-Linear Refractive Indices.* Journal of Non-Crystalline Solids. 239:139-142.

[64] K. S. Bindra, H. T. Bookey, A. K. Kar, S. S. Wherrett. 2001. *Nonlinear Optical Properties of Chalcogenide Glasses: Observation of Multiphoton Absorption.* Applied Physics Letters. 79(13):1939-1941.

[65] M. Asobe. 1997. *Nonlinear Optical Properties of Chalcogenide Glass Fibers and Their Application to All-Optical Switching.* Optical Fiber Technology. 3:142-148.

[66] T. Cardinal, K. A. Richardson, H. Shim, A. Schulte, R. Beatty, K. Le Foulgoc, C. Meneghini, J. F. Viens, A. Villeneuve. 1999. *Non-Linear Optical Properties of Chalcogenide Glass in the System As-S-Se.* Journal of Non-Crystalline Solids. 256&257:353-360.

[67] UDT Sensors Inc. *Optoelectronic Components Catalog.*

[68] D. McMorrow, W. T. Lotshaw, G. A. Kenney-Wallace. 1988. *Femtosecond Optical Kerr Studies on the Origin of the Nonlinear Response in Simple Liquids.* IEEE Journal of Quantum Electronics. 24(2):443-454.

[69] A. Jha, X. Liu, A. K. Kar, H. T. Bookey. 2001. *Inorganic Glasses as Kerr-Like Media.* Current Opinion in Solid State & Materials Science. 5:475-479

[70] J. Riquejo-Isidro, A. K. Mairaj, V. Pruneri, D. W. Hewak, M. C. Netti, J. J. Baumberg. 2003. *Self Refractive Non-linearities in Chalcogenide Based Glasses.* Journal of Non-Crystalline Solids. 317(3):241.246.

[71] K. A. Cerqua-Richardson, J. M. McKinley, B. Lawrence, S. Joshi, A. Villeneuve. 1998. *Comparison of Nonlinear Optical Properties of Sulfide Glasses in Bulk and Thin Film Form.* Optical Materials. 10:155-159.

[72] S. Spalter, H. Y. Hwang, J. Zimmermann, G. Lenz, T. Katsufuji, S.-W. Cheong, R. E. Slusher. 2002. *Strong Self-Phase Modulation in Planar Chalcogenide Glass Waveguides.* Optics Letters. 27(5):363-365.

[73] A. C. van Popta, R. G. DeCorby, C. J. Haugen, T. Robinson, J. N. McMullin. 2002. *Photoinduced refractive index change in As2Se3 by 633nm illumination.* Optics Express. 10(15):639:644.

[74] C. Kalpouzos, W. T. Lotshaw, D. McMorrow, G. A. Kenney-Wallace. 1987. *Femtosecond laser-induced Kerr responses in liquid CS_2.* Journal of Physical Chemistry. 91:2028.

[75] Y. Ruan, B. Luther-Davies, W. Li, A. Rode, V. Kolev, S. Madden. 2005. *Large phase shifts in As_2Se_3 waveguides for all-optical processing devices.* Optics Letters. 30(19):2605-2607.

[76] K. Suzuki, K. Ogusu. 2005. *Single-mode Ag-As_2Se_3 strip-loaded waveguides for applications to all-optical devices.* Optics Express. 13(21):8634-8641.

[77] M. Frumar, T. Wagner. 2003. *Ag doped chalcogenide glasses and their applications.* Current Opinion in Solid State & Materials Science. 7:117-126.

[78] Y-F Chen, K. Beckwitt, F.W. Wise, B.G. Aitken, J.S. Sanghera, I.D. Aggarwal. 2006. *Measurement of fifth- and seventh-order nonlinearities of glasses.* Journal of Optical Society of America B. 23(2):347-352.

[79] G. Bodebs, S. Cherukulappurath, H. Leblond, J. Troles, F. Smektala, F. Sanchez. 2003. *Experimental and theoretical study of higher-order nonlinearities in chalcogenide glasses.* Optics Communications. 219:427-433.

APPENDIX A *Derivation of DOKE Equations*

The following is a matrix algebra derivation of the DOKE formulations given section §3.2. This derivation is originally presented in Reference 27. Matrix representations of each of the optical components used are defined in the following table.

Optical Element	Matrix Representation	Description
Quarter-Wave Plate	$\begin{bmatrix} i & 0 \\ 0 & 1 \end{bmatrix}$	Fast axis aligned 45° to the horizontal
Polarizer	$\begin{bmatrix} 0 \\ 1 \end{bmatrix}$	Allows only vertically polzrized omponent of light to pass through
Analyzer	$\begin{bmatrix} 1 & 0 \end{bmatrix}$	Allows only horizontally polzrized omponent of light to pass through
Wollaston Prism	$\begin{bmatrix} 1 & 1 \end{bmatrix}$	Separates horizontal and vertical polarization components of light
Sample	$\begin{bmatrix} 1 & 0 \\ 0 & e^{i\phi} \end{bmatrix}$	Produces a phase retardation ϕ
45°- Rotation Matrix	$\frac{1}{\sqrt{2}}\begin{bmatrix} 1 & -1 \\ 1 & 1 \end{bmatrix}$	Rotation of 45 degrees
δ - Rotation Matrix	$\begin{bmatrix} \cos\delta & -\sin\delta \\ \sin\delta & \cos\delta \end{bmatrix}$	Rotation of δ degrees. General rotation matrix.

TABLE A.1. Matrix representation of various optical elements used in the DOKE setup.

In the DOKE setup, the pump beam polarized at 45° incident on the sample induces a birefringence of $\delta\phi = \phi' + i\phi''$, where ϕ' and ϕ'' are the real and imaginary components of the phase retardation, respectively. This is detected by monitoring the phase retardation of a circularly polarized probe beam with the differential photodetector setup described in Chapter 3. The arrangement is: Polarizer - Quarter-Wave Plate - Sample - Wollaston Prism - Detector (see Figure 3.1). The detector signal matrix is given by

$$D = \frac{1}{2}\begin{bmatrix} 1 & 1 \\ -1 & 1 \end{bmatrix}\begin{bmatrix} 1 & 0 \\ 0 & e^{i\phi} \end{bmatrix}\begin{bmatrix} 1 & 0 \\ 0 & i \end{bmatrix}\begin{bmatrix} 1 & -1 \\ 1 & 1 \end{bmatrix}\begin{bmatrix} 0 \\ 1 \end{bmatrix} \qquad \text{(Eq. A.1)}$$

$$D = \begin{bmatrix} D_x \\ D_y \end{bmatrix} = \frac{1}{2}\begin{bmatrix} -1 + ie^{i\phi} \\ 1 + ie^{i\phi} \end{bmatrix}. \qquad \text{(Eq. A.2)}$$

Separating the x and y components with the Wollaston prism yields

$$I_x = D_x D_x^* = \frac{1}{4}(-1 + ie^{-i\phi})(-1 - ie^{-i\phi^*})$$

$$= \frac{1}{4}(1 + ie^{-i\phi'}e^{-\phi''} - ie^{i\phi'}e^{-\phi''} + e^{i\phi' - \phi'' - i\phi' - \phi''})$$

$$= \frac{1}{4}(1 + ie^{-i\phi''}(e^{-i\phi'} - e^{i\phi'}) + e^{-2\phi''})$$

$$= \frac{1}{4}(1 - 2i^2 \sin\phi' e^{-\phi''} + e^{-2\phi''})$$

$$I_x = \frac{1}{4}(1 + e^{-2\phi''}) + \frac{1}{2}\sin\phi' e^{-\phi''} \qquad \text{(Eq. A.3)}$$

$$I_y = D_y D_y^* = \frac{1}{4}(1 + ie^{i\phi})(1 - ie^{-i\phi^*})$$

$$= \frac{1}{4}(1 - ie^{-i\phi'}e^{-\phi''} + ie^{i\phi'}e^{-\phi''} + e^{i\phi' - \phi'' - i\phi' - \phi''})$$

$$= \frac{1}{4}(1 + ie^{-i\phi''}(-e^{-i\phi'} + e^{i\phi'}) + e^{-2\phi''})$$

$$= \frac{1}{4}(1 + 2i^2 \sin\phi' e^{-\phi''} + e^{-2\phi''})$$

$$I_y = \frac{1}{4}(1 + e^{-2\phi''}) - \frac{1}{2}\sin\phi' e^{-\phi''} \qquad \text{(Eq. A.4)}$$

$$I_x + I_y = \frac{1}{2}(1 + e^{-2\phi''}) = \frac{1}{2}e^{-\phi''}(e^{\phi''} + e^{-\phi''}) = e^{-\phi''}\cosh\phi''$$

$$I_x - I_y = \sin\phi' e^{-\phi''}$$

$$\frac{I_x - I_y}{I_x + I_y} = \frac{\sin\phi'}{\cosh\phi''}. \qquad \text{(Eq. A.5)}$$

In the absence of large nonlinear absorption, as in chalcogenide glasses where β is usually very small at the wavelength of interest, $\phi'' \approx 0$. The Equation A.5 in this case simplifies to

$$\frac{I_x - I_y}{I_x + I_y} = \sin\phi' \approx \phi' \text{ for small } \phi'. \qquad \text{(Eq. A.6)}$$

In the second DOKE condition, with pump beam polarized at 0°, the detector signal matrix is given by

$$D = \frac{1}{2}\begin{bmatrix} 1 & 0 \\ 0 & e^{i\phi} \end{bmatrix}\begin{bmatrix} 1 & 1 \\ -1 & 1 \end{bmatrix}\begin{bmatrix} 1 & 0 \\ 0 & i \end{bmatrix}\begin{bmatrix} 1 & -1 \\ 1 & 1 \end{bmatrix}\begin{bmatrix} 0 \\ 1 \end{bmatrix} \qquad \text{(Eq. A.7)}$$

$$D = \begin{bmatrix} D_x \\ D_y \end{bmatrix} = \frac{1}{2}\begin{bmatrix} -1+i \\ e^{i\phi} + ie^{i\phi} \end{bmatrix}. \qquad \text{(Eq. A.8)}$$

Separating the x and y components with the Wollaston prism yields

$$I_x = D_x D_x^* = \frac{1}{4}(-1+i)(-1-i) = \frac{1}{4}(1+i-i+1)$$

$$I_x = \frac{1}{2} \qquad \text{(Eq. A.9)}$$

$$I_y = D_y D_y^* = \frac{1}{4}(e^{i\phi} + ie^{i\phi})(e^{-i\phi^*} - ie^{-i\phi^*})$$

$$= \frac{1}{4}(e^{i\phi - i\phi^*} + ie^{i\phi - i\phi^*} - ie^{i\phi - i\phi^*} + e^{i\phi - i\phi^*})$$

$$I_y = \frac{1}{4}(2e^{i\phi' - \phi'' - i\phi' - \phi''}) = \frac{1}{2}e^{-2\phi''} \qquad \text{(Eq. A.10)}$$

$$I_x - I_y = \frac{1}{2} - \frac{1}{2}e^{-2\phi''} = \frac{1}{2}e^{-\phi''}(e^{\phi''} - e^{-\phi''}) = e^{-\phi''}\sinh\phi''$$

$$I_x - I_y = \frac{1}{2} + \frac{1}{2}e^{-2\phi''} = \frac{1}{2}e^{-\phi''}(e^{\phi''} + e^{-\phi''}) = e^{-\phi''}\cos h\phi''$$

$$\frac{I_x - I_y}{I_x + I_y} = \tanh\phi'' \qquad \text{(Eq. A.11)}$$

As expected, the expression is zero in the absence of absorptive terms. Together with Equation A.6, both real and imaginary terms of the phase retardation ϕ can be extracted. Thus, the DOKE detection technique leads to simple expressions in the phase retardation and allows for easy determination of the Kerr and two-photon absorption coefficients, n_2 and β.

Only two polarization conditions of the pump beam have been described above. Polarization at 0° and 45°. However, there are four useful polarization conditions in DOKE detection. Pumping at the polarization of 45° has been shown to yield a signal given by Equation A.5. Similarly, it can be shown that pumping at a polarization of -45° simply yields a negative of Equation A.5. The second, 0°, polarization condition has been shown to yield a signal given by Equation A.11. Likewise, it can be shown that pumping with polarization of 90° yields a signal that is negative of Equation A.11. Therefore, there are four useful polarization conditions in the DOKE technique, -45°,0°,45° and 90°.

APPENDIX B *Nonlinear Phaseshift Calculation*

With every Kerr scan, the data from the lock-in amplifiers is recorded on the computer. The recorded variables are the computer controlled stage position, differential photodetector readings A-B and A+B, and the probe beam reference photodetector *Ref*. The dynamic range readout of the lock-in amplifiers is between 0 and 5, where reading of 5 represents a voltage reading that is one half of the current sensitivity setting. i.e. if the sensitivity is at 100mV, a 0-5 output represents 0-50mV scale. Consequently, the actual recorded value *(V)* is obtained by multiplying the lock-in amplifier reading by the set sensitivity *(Sens)*, and dividing by 10.

$$V = \frac{Reading \times Sens}{10} \qquad \text{(Eq. B.1)}$$

The ratio of the detected signals A-B and A+B, as given by Equation 3.5 is

$$\frac{A-B}{A+B} = \sin\phi' . \qquad \text{(Eq. B.2)}$$

The real part of the nonlinear phaseshift is then obtained with

$$\phi' = \frac{(A-B) \times Sens_{(A-B)}/10}{(A+B) \times Sens_{(A+B)}/10} . \qquad \text{(Eq. B.3)}$$

Typically, ϕ' is small $(\phi' < 0.1)$, hence approximation $\sin\phi' \approx \phi'$ is used.

Similarly, for the nonlinear absorption scan, the ratio of the detected signals A-B and A+B, as given by Equation 3.4 is

$$\frac{A-B}{A+B} = \tanh\phi'', \qquad \text{(Eq. B.4)}$$

and the imaginary part of the nonlinear phaseshift is calculated the same way as given by Equation B.3:

$$\phi'' = \frac{(A-B)\times Sens_{(A-B)}/10}{(A+B)\times Sens_{(A+B)}/10}, \qquad \text{(Eq. B.5)}$$

with the approximation $\phi'' \approx \tanh\phi''$ for small ϕ''. In both cases, the "A-B" signal is also divided by the normalized reference detector signal. This is done for the purpose of reducing noise in the recorded Kerr signal, which comes from intensity fluctuations of the OPA laser light.

APPENDIX C *Calculations with Reference Sample*

Since fused silica is a material with well documented Kerr coefficient value, it was chosen as a reference sample in the DOKE setup. A Kerr scan of a fused silica is always performed just before or immediately after a Kerr scan of a thin film sample, giving us a reference point for extracting the sample's Kerr coefficient n_2. This way, the accuracy of the results becomes less prone to possible day to day variations of laser alignment, than using absolute values for the recorded nonlinear phaseshift. The n_2 is then calculated as follows.

The real component of the nonlinear phaseshift as given by Equation 3.1 is

$$\phi' = 2\pi\frac{n_2 d}{\lambda} I_{pump}. \qquad \text{(Eq. C.1)}$$

Taking the ratio of the nonlinear phaseshifts obtained from the Kerr scan of the reference sample and the thin film sample ϕ'_S/ϕ'_R, gives

$$\frac{\phi'_S}{\phi'_R} = \frac{(n_{2S})(I_S)(d_S)}{(n_{2R})(I_R)(d_R)}, \qquad \text{(Eq. C.2)}$$

and the Kerr coefficient of the sample is calculated using

$$n_{2S} = n_{2R}\frac{(\phi'_S)(d_R)(I_R)}{(\phi'_R)(d_S)(I_S)}. \qquad \text{(Eq. C.3)}$$

d_S and d_R are the thicknesses of the thin film and fused silica samples, respectively, and n_{2R} is the Kerr coefficient of fused silica. Typically, the pump beam intensity for the thin

film and reference Kerr scans would be kept the same, thus $I_S = I_R$. However, since the OPA laser power tends to fluctuate a small but noticeable amount even over a short period of time, the two variables are left in the expression for improved accuracy.

APPENDIX D

Sample Results and Calculations

D.0.1 Separating the Kerr response of the thin film from its substrate.

Since we are working with thin film samples, the recorded nonlinear phaseshift ϕ'_{Samp} is a sum of nonlinear phaseshifts accumulated not only through the thin film ϕ'_{Flm} but also the substrate ϕ'_{Sub}.

$$\phi'_{Samp} = \phi'_{Sub} + \phi'_{Flm}. \qquad \text{(Eq. D.1)}$$

Here, ϕ'_{Sub} cannot be neglected. Even though the n_2 of the substrate may seen insignificantly small, its accumulated nonlinear phaseshift might be comparable to that of the thin film, since the substrate is typically ~1000 times thicker than the film. If a separate Kerr scan is performed on the substrate only, ϕ'_{Flm} can be isolated.

Dividing Equation D.1 by ϕ'_{Sub}

$$\frac{\phi'_{Flm}}{\phi'_{Sub}} = \left[\frac{\phi'_{Samp}}{\phi'_{Sub}} - 1\right]. \qquad \text{(Eq. D.2)}$$

From Equation C.3 we have

$$\frac{n_{2Flm}}{n_{2Sub}} = \frac{(\phi'_{Flm})(d_{Sub|})(I_{Sub})}{(\phi'_{Sub})(d_{Flm})(I_{Flm})}. \qquad \text{(Eq. D.3)}$$

Combining Equation D.2 and Equation D.3 we get:

$$\frac{n_{2Flm}}{n_{2Sub}} = \left[\frac{\phi'_{Samp}}{\phi'_{Sub}} - 1\right]\frac{(d_{Sub})(I_{Sub})}{(d_{Flm})(I_{Flm})} \qquad \text{(Eq. D.4)}$$

Together with reference sample scan (see Appendix B) we find n_{2Flm}:

$$\frac{n_{2Flm}}{n_{2R}} = \frac{n_{2Flm}}{n_{2Sub}} \times \frac{n_{2Sub}}{n_{2R}} = \left[\frac{\phi'_{Samp}}{\phi'_{Sub}} - 1\right]\frac{(d_{Sub})(I_{Sub})}{(d_{Flm})(I_{Flm})} \times \frac{(\phi'_{Sub})(d_R)(I_R)}{(\phi'_R)(d_{Sub})(I_{Sub})}$$

$$\frac{n_{2Flm}}{n_{2R}} = \left[\frac{\phi'_{Samp}}{\phi'_{Sub}} - 1\right]\frac{(\phi'_{Sub})(d_R)(I_R)}{(\phi'_R)(d_{Flm})(I_{Flm})}. \qquad \text{(Eq. D.5)}$$

D.0.2 Sample Results

Table D.1 lists a sample data for As_2Se_3 thin film sample deposited on a BK-7 glass substrate. The table includes Kerr scans of the fused silica (reference) sample, the As_2Se_3 film and the film substrate. The three scans are recorded in close succession. Also given is a sample result for the second polarization condition of the pump beam ($\theta = 0°$), which gives the imaginary part of the nonlinear phase shift.

Sample	Sample Thickness	Avg. Pump Power (mW)	Phase Shift
Fused Silica	1.66mm	2.56	$\phi' = 0.0185$
Film & Substrate	16μm (film only)	2.61	$\phi' = 0.0686$
Substrate	1.51mm	2.59	$\phi' = 0.0233$
Film & Substrate	16μm (film only)	2.37	$\phi'' = 0.0021$

TABLE D.1. Sample results recorded for consecutive Kerr scans of fused silica, thin film sample and film substrate.

The pump beam intensity is given by

$$I = \frac{Power}{Area} = \frac{P_{avg} \times Period}{PulseDuration}/Area, \qquad \text{(Eq. D.6)}$$

where

$$Period = (1080Hz)^{-1}, \quad \text{(Eq. D.7)}$$

$$PulseDuration = FWHM/\sqrt{2} = 125fs/\sqrt{2}, \quad \text{(Eq. D.8)}$$

$$\text{and } Area = \pi\left[\frac{1}{2}\omega_o\right]^2 = \pi\left[\frac{1}{2}(590\mu m)\right]^2. \quad \text{(Eq. D.9)}$$

Using Equation D.5, n_2 for the As_2Se_3 thin film sample can now be calculated:

$$n_{2Film} = 2.68\times10^{-20}\times\left[\frac{0.0686}{0.0233}-1\right]\frac{(0.0233)(1.66mm)(2.56)}{(0.0185)(16\mu m)(2.61)}m^2/W \quad \text{(Eq. D.10)}$$

$$\boxed{n_{2Film} = 6.68\times10^{-18}m^2/W} \quad \text{(Eq. D.11)}$$

The two photon absorption coefficient β is calculated by re-arranging Equation 3.2:

$$\beta = \frac{\phi''}{dI_{Pump}}. \quad \text{(Eq. D.12)}$$

$$\beta = \frac{0.0021}{16\mu m}\left[\frac{1080Hz\times125fs}{2.37mW\times\sqrt{2}}\times\pi\left[\frac{1}{2}(590\mu m)\right]^2\right]m/W \quad \text{(Eq. D.13)}$$

$$\boxed{\beta = 0.14\times10^{-11}m/W} \quad \text{(Eq. D.14)}$$